

Autonomous error correction of a single logical qubit using two transmons

Ziqian Li^{‡,1,2,3} Tanay Roy^{‡,1,2,*} David Rodríguez Pérez,⁴
Kan-Heng Lee,^{1,2,†} Eliot Kapit,⁴ and David I. Schuster^{1,2,5,3}

¹*James Franck Institute, University of Chicago, Chicago, Illinois 60637, USA*

²*Department of Physics, University of Chicago, Chicago, Illinois 60637, USA*

³*Department of Applied Physics, Stanford University, Stanford, California 94305, USA[‡]*

⁴*Department of Physics, Colorado School of Mines, Golden, Colorado 80401, USA*

⁵*Pritzker School of Molecular Engineering, University of Chicago, Chicago, Illinois 60637, USA*

(Dated: February 15, 2023)

Large-scale quantum computers will inevitably need quantum error correction to protect information against decoherence. Traditional error correction typically requires many qubits, along with high-efficiency error syndrome measurement and real-time feedback. Autonomous quantum error correction (AQEC) instead uses steady-state bath engineering to perform the correction in a hardware-efficient manner. We realize an AQEC scheme, implemented with only two transmon qubits in a 2D scalable architecture, that actively corrects single-photon loss and passively suppresses low-frequency dephasing using six microwave drives. Compared to uncorrected encoding, factors of 2.0, 5.1, and 1.4 improvements are experimentally witnessed for the logical zero, one, and superposition states. Our results show the potential of implementing hardware-efficient AQEC to enhance the reliability of a transmon-based quantum information processor.

I. INTRODUCTION

Quantum error correction (QEC) is critical for performing long computations involving many qubits, such as Shor’s [1] or quantum chemistry algorithms [2]. Errors accumulating in the quantum system can be regarded as entropy or heat entering the system. In this context, the standard measurement and feedback-based QEC methods can be thought of us creating a “Maxwell Demon” keeping the system cold. These methods typically require many qubits and complex control hardware and have been demonstrated approaching the fault tolerance threshold [3–12]. When cooling atoms, rather than using measurement-based feedback, typically laser cooling is used. In laser cooling, the measurement and feedback are effectively encoded in the internal level structure and clever choice of laser drives. Along these lines, it is possible to perform autonomous quantum error correction (AQEC) where rather than measurements and gates, the system is “cooled” via an appropriate set of drives and couplings to engineered thermal reservoirs [13]. Like laser cooling, AQEC can dramatically simplify the quantum and classical hardware and control required. Both autonomous and feedback-based QEC are more challenging than simply cooling because they require that the cooling process preserves the logical manifold of the system.

AQEC has received growing attention in theoretical proposals [14–22]. In addition to the usual QEC conditions [23], AQEC requires that the error-correction op-

erations must commute with the system Hamiltonian at all times. This makes AQEC most appropriate for hardware efficient [24–29] systems with constrained error syndromes. Thus far all demonstrations, have encoded the logical qubits into 3D superconducting cavities using an ancilla qubit as a control [24, 27].

In this report, we experimentally realize AQEC in a pure transmon-based [30] system using scalable on-chip circuit structures. We propose a new AQEC protocol, called the Star code, which simplifies the original very small logical qubit (VSLQ) proposal [16, 18] and does not require four-photon drive terms. We develop a coherence-preserving two-transmon coupler that can parametrically generate all interactions needed for the protocol. With AQEC turned on, the logical states show higher coherence times than the uncorrected case. The structure of the paper is as follows. First, we explain the logical encoding and Hamiltonian construction of the Star code. Then we experimentally calibrate each of the parametric processes used in the code. Finally, we prepare the logical states and characterize the coherence improvement.

II. THEORY

The Star code encodes a logical qubit using two orthogonal states in a nine-dimensional (two-qutrit) Hilbert space as $|L_0\rangle = (|gf\rangle - |fg\rangle)/\sqrt{2}$ (logical “zero”), and $|L_1\rangle = (|gg\rangle - |ff\rangle)/\sqrt{2}$ (logical “one”) where $|g\rangle$, $|e\rangle$, and $|f\rangle$ represent the lowest three energy levels of a transmon. The error states after a single photon-loss (one transmon in $|e\rangle$) are orthogonal to the logical space and to each other. Further, both logical states have an equal expected photon number so that photon loss does not reveal information about the state it was emitted from. We engineer a parent Hamiltonian for the logical states through $|gf\rangle\langle fg|$ and $|gg\rangle\langle ff|$ paramet-

* Present address: Superconducting Quantum Materials and Systems Center, Fermi National Accelerator Laboratory (FNAL), Batavia, IL 60510, USA

† Present address: Advanced Quantum Testbed, Lawrence Berkeley National Laboratory, Berkeley, CA 94720, USA

‡ These authors contributed equally to this work

ric processes. These processes are all implemented by driving through $|ee\rangle$ as an intermediate state, producing the star topology in Hilbert space that gives the code its name (see Fig. 1a). Using an intermediate state allows these to be achieved using only 2-photon drives (QQ sidebands) rather than the higher-order 4-photon processes required by the VSLQ [18]. Despite both sets of drives going through $|ee\rangle$, with careful tuning of the drive W , the logical states can be made dark with respect to $|ee\rangle$ by detuning the $|L_0\rangle$ ($|L_1\rangle$) sidebands by $\pm\nu_r$ ($\pm\nu_b$). When all of these processes are simultaneously applied, the two-transmon Hamiltonian in the logical-static frame (see Appendix B for derivation) is

$$\tilde{H}_{QQ} = \frac{W}{2} (|ee\rangle\langle gf| e^{2\pi i\nu_r t} + |ee\rangle\langle fg| e^{2\pi i\nu_r t} + |ee\rangle\langle gg| e^{2\pi i\nu_b t} + |ee\rangle\langle ff| e^{2\pi i\nu_b t}) + h.c. \quad (1)$$

Each transmon Q_j is coupled to a lossy resonator R_j , which acts as the cold reservoir for entropy dumping. A single-photon loss, the dominant source of error in the system, populates the $|e\rangle$ level, triggering autonomous correction enabled by two transmon-resonator (QR) error correcting sidebands $|e0\rangle_j \leftrightarrow |f1\rangle_j, j = 1, 2$ (right part of Fig. 1a). These sidebands are applied resonantly at rates Ω_j to the system, adding \tilde{H}_{QR_j} to the system Hamiltonian H_{static} ,

$$\tilde{H}_{QR1} = \frac{\Omega_1}{2} a_{r1}^\dagger (|fg\rangle\langle eg| + |ff\rangle\langle ef|) \otimes I_4 + h.c.,$$

$$\tilde{H}_{QR2} = \frac{\Omega_2}{2} a_{r2}^\dagger (|gf\rangle\langle ge| + |ff\rangle\langle fe|) \otimes I_4 + h.c., \quad (2)$$

$$\tilde{H}_{\text{static}} = \tilde{H}_{QQ} \otimes I_4 + \sum_{j=1,2} \tilde{H}_{QR_j} + H_c. \quad (3)$$

Here a_{rj} is the annihilation operator for the j -th resonator, and α_j is the anharmonicity of j -th transmon. H_c contains the diagonal terms from frame transformation. We label the full state as $|Q_1 Q_2 R_1 R_2\rangle$. We keep the lowest two levels for each resonator, and I_n is the $n \times n$ identity matrix.

The Star code can correct the loss of a single photon from one of the qubits. Suppose Q_1 loses a photon at rate $2\gamma_1$, where γ_1 is the $|e\rangle \rightarrow |g\rangle$ decay rate. The logical $|L_0 00\rangle$, consequently, becomes the error state $|E_{01} 00\rangle = |eg 00\rangle$ with energy $-\frac{\alpha_1}{2}$. When $W \gg \Omega_j$, \tilde{H}_{QR_j} is a perturbation and only drives the transition $|E_{01} 00\rangle \leftrightarrow |L_0 10\rangle$ (See Fig. 1 (a)). Assuming the resonator's decay rate $\kappa_1 \gg \gamma_1$, this oscillation quickly damps back to the original logical state $|L_0 00\rangle$ with no extra phase accumulated, and completes the correction cycle. The correction procedure for $|L_1\rangle$ is similar through an independent path. The logical superposition state preserves relative phases since the QR sidebands do not distinguish the correction path. Such a two-step logical refilling rate can be approximated with Fermi's golden rule $\Gamma_{Rj} \simeq \frac{\Omega_j^2 \kappa_j}{\Omega_j^2 + 2\kappa_j^2}$ [31]. Apart from providing protection against single-photon loss, the star code also provides

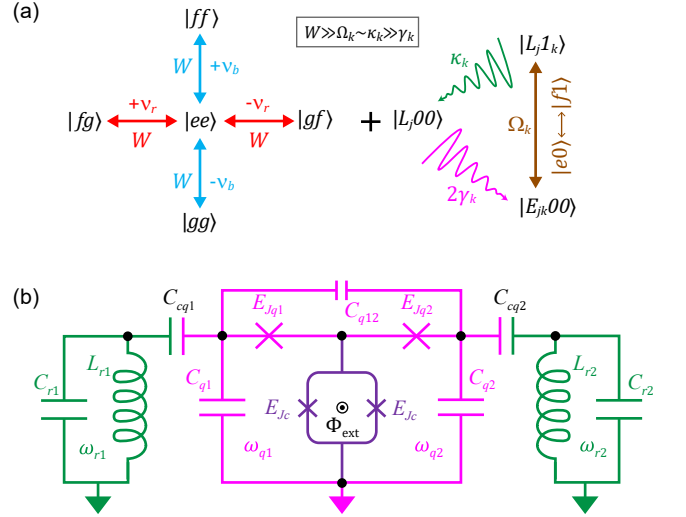


FIG. 1. Schematic of Star code and circuit implementation. (a) Illustration of the autonomous error-correction scheme. The protocol requires simultaneous application of two QQ blue sidebands ($|ee\rangle \leftrightarrow |gg\rangle$ and $|ee\rangle \leftrightarrow |ff\rangle$), two QQ red sidebands ($|ee\rangle \leftrightarrow |fg\rangle$ and $|ee\rangle \leftrightarrow |gf\rangle$), and two QR error correcting sidebands ($|e0\rangle \leftrightarrow |f1\rangle$). All six drives are always-on. The red and blue QQ sidebands have nominally equal rates W with equal and opposite detunings from the on-resonance values. The right part describes the AQEC cycle when a single-photon-loss event occurs. Logical state $|L_j 0_0\rangle$ loses a photon from transmon Q_k at rate $2\gamma_k$ and becomes the error state $|E_{jk} 0_0\rangle$. QR error correcting sidebands bring the state at rate Ω_k to $|L_j 1_k\rangle$ with one photon populating R_k . R_k 's photon decays quickly (at a rate κ_k) and recover the original logical state. (b) Circuit diagram for AQEC implementation. The device consists of two transmons, two resonators, and an inductive coupler.

suppression to $1/f$ dephasing error [18, 32]. The continuous QQ drives create an energy gap between the logical manifold and all other states, suppressing low-frequency noise. Theoretical lifetime improvement of logical states is further discussed in Ref. [33].

We realize this protocol using the circuit shown in Fig. 1b. The key component is the inductive coupler based on the design in Ref. [34] that enables the realization of fast parametric interactions. Two transmons Q_1 and Q_2 serve as the qutrits and share a common path to ground. This path is interrupted by a Superconducting Quantum Interference Device (SQUID) loop. The SQUID functions as a tunable inductor with external DC and RF magnetic fields threaded for activating the QQ sidebands. Each transmon is capacitively coupled to a lossy resonator serving both as the readout and cold reservoir. QR sidebands can be performed by sending a charge drive at the half transition frequency to the transmon [35]. Full circuit quantization is shown in Appendix C.

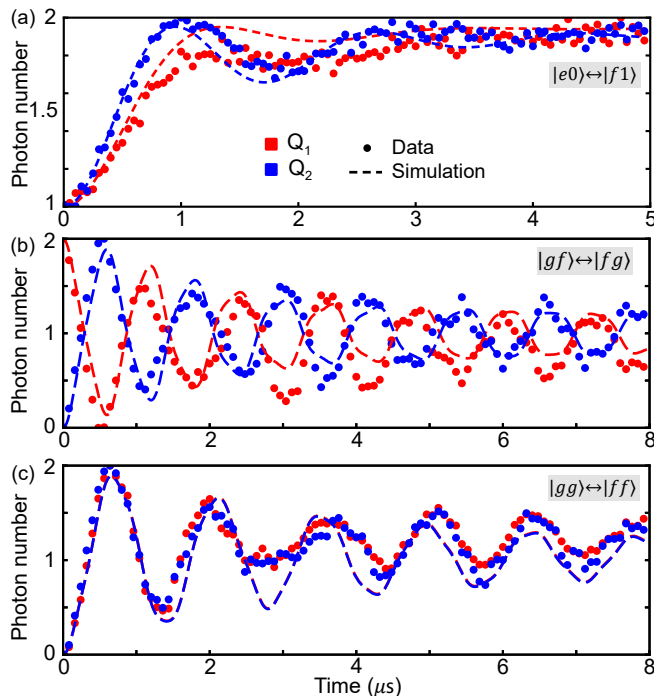


FIG. 2. Different parametric oscillations. (a) Error correcting QR sidebands $|e0\rangle \leftrightarrow |f1\rangle$ applied separately at rates $\Omega_1 = 0.49$ MHz and $\Omega_2 = 0.59$ MHz to the transmon-resonator pairs with $|e\rangle$ as initial states. Effective transitions (b) $|gf\rangle \leftrightarrow |fg\rangle$ and (c) $|gg\rangle \leftrightarrow |ff\rangle$ are measured when all QQ and QR sidebands are simultaneously turned on. Extracted sideband rates and detunings from simulation are $W_r = 1.45$ MHz, $W_b = 1.25$ MHz, $\nu_r = 0.8$ MHz, $\nu_b = -0.9$ MHz, $\Omega_1 = \Omega_2 = 0.39$ MHz. Oscillation distortions are quantitatively matched in the lab frame simulations.

III. EXPERIMENTAL RESULTS

A. Device implementation and sideband calibration

In this section, we will characterize the individual qubits and realize the required sidebands to create and correct the logical states. We adjust the DC flux point to minimize the Cross-Kerr coupling between transmons which can dephase the logical superposition states (See Appendix D for further discussion). The measured Cross-Kerr couplings are all lower than 320 kHz while maintaining Ramsey dephasing times $T_{R_{ge}} = 15.2(9.8)$ μ s with relaxation time $T_{1_{ge}} = 24.3(9.1)$ μ s, for $Q_1(Q_2)$ (See Appendix A).

To calibrate the QR sidebands for selective photon pumping, we initialize the system in $|eg00\rangle$ and apply a continuous charge drive at frequency $(\omega_{r1} + \omega_{q1} + \alpha_1)/2$ to activate a 2-photon $|e0\rangle \leftrightarrow |f1\rangle$ transition between Q_1 and R_1 at a rate of 0.49 MHz. The system achieves a steady state $|fg00\rangle$ within 3 μ s as shown by red points in Fig. 2(a). Similarly, a 0.59 MHz QR2 drive takes $|ge00\rangle$ to $|gf00\rangle$ in a similar time (blue points in Fig. 2(a)). The decay of transmon reduces the final average photon

number slightly below 2.

We achieve at least 20 MHz QQ red sidebands ($|j, k\rangle \leftrightarrow |j+1, k-1\rangle$) and 5 MHz QQ blue sidebands ($|j, k\rangle \leftrightarrow |j+1, k+1\rangle$) separately at the operating point, demonstrating a fast, coherence-preserved two-qutrit coupler with suppressed ZZ interaction. Blue sidebands have a slower rate limited by stray signals from higher flux modulation frequencies (See discussion in Appendix E). All possible sidebands realized in this coupler are shown in Appendix F.

By driving all six sidebands, the core effective 4-photon processes, $|fg\rangle \leftrightarrow |gf\rangle$ and $|gg\rangle \leftrightarrow |ff\rangle$ and the error-correcting QR drives can be realized simultaneously. In practice, the QQ red and blue sideband rates ($W_r = 1.45$ MHz and $W_b = 1.25$ MHz) are slightly different. When applying all sidebands, we choose a smaller W , because the coupler was found to heat and shift the readout resonator when driven at larger rates making tomographic reconstruction inaccurate. We choose almost opposite detunings ($\nu_r = 0.8$ MHz, $\nu_b = -0.9$ MHz) for larger energy separation of the eigenstates and better error correction performance. Both QR sidebands are turned on at rates $\Omega_1 = \Omega_2 = 0.39$ MHz. Fig. 2(b) shows the evolution when the initial state is $|gf\rangle$. The average photon number of Q_1 (in red) and Q_2 (in blue) are read out simultaneously, and the oscillation between 0 and 2 forms an effective 4-photon red sideband. Note that this effective swap process is slightly different from the direct $|fg\rangle \leftrightarrow |gf\rangle$ transition as the population in $|ee\rangle$ will appear intermediately when the initial state has overlap with the eigenstates that have $|ee\rangle$ component. Under this condition, $|ee\rangle$ is no longer the dark state of the mixed QQ sidebands. Oscillation damping originates from the detuning-induced slow interference and decoherence of the qutrit subspace, and this distortion is captured by the simulation as well. Similarly, by choosing the initial state as $|gg\rangle$, the effective four-photon blue sideband $|gg\rangle \leftrightarrow |ff\rangle$ can be observed in Fig. 2(c).

B. Error Correction Performance

The logical state initialization requires sequential application of multiple single-qutrit and two-qutrit rotations. For $|L_0\rangle$ and $|L_1\rangle$, QQ red and blue sidebands are used to generate entanglement, and for $|L_x\rangle = (|L_0\rangle + |L_1\rangle)/\sqrt{2} = (|g\rangle + |f\rangle)(|g\rangle - |f\rangle)/2$, only single qutrit rotations are required. The preparation times for initial states are separately 313 ns, 142 ns, and 282 ns for $|L_0\rangle$, $|L_1\rangle$ and $|L_x\rangle$. The detailed preparation circuit is discussed in Appendix G. We perform full two-qutrit state tomography [36, 37] and obtain initial state fidelities of 88.1%, 89.1% and 88.7% for the three states respectively. The tomography sequences and density matrix reconstruction are shown in Appendix H.

We characterize the performance of the Star code by comparing three different cases — free decay, QQ sideband spin-locking (4 QQ echo), and full AQEC. For

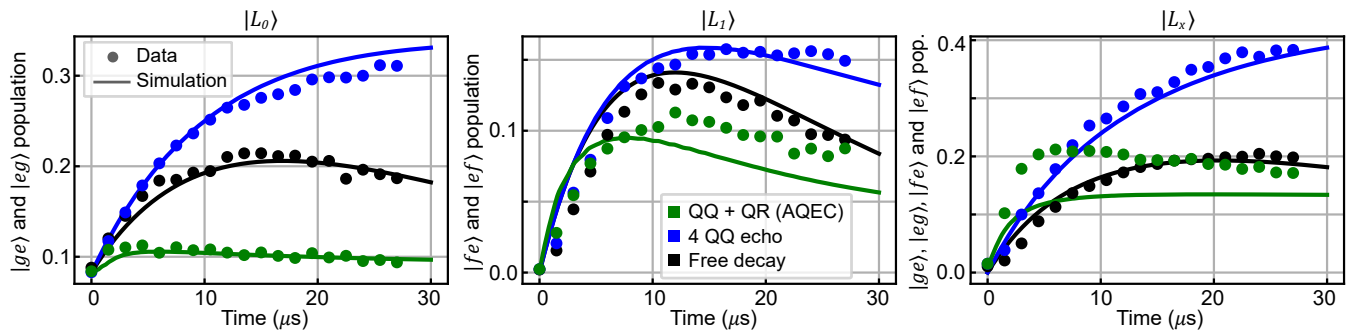


FIG. 3. Error population under different conditions. Black, blue, and green points represent tomographic measurement results under free decay, 4 QQ echo, and full AQEC. The y-axes represent the combined population of error states for initial states $|L_0\rangle$, $|L_1\rangle$, and $|L_x\rangle$. Population accumulates at the error states in the free decay case, enhanced in the 4 QQ echo case, and corrected with AQEC drive on. The experimental data is explained with master equation simulations. Detailed simulation parameters are shown in the Appendix I.

free decay, we do not apply any drive after the state preparation. For the 4 QQ echo case, we turn on the QQ sidebands $|ee\rangle \leftrightarrow \{|gf\rangle, |fg\rangle, |gg\rangle, |ff\rangle\}$ with a similar rate-detuning configuration as shown in Fig. 1a ($W_r = 1.0$ MHz, $W_b = 1.7$ MHz, $\nu_r = 1.5$ MHz, $\nu_b = 0.0$ MHz). This case shows coherence improvement from spin-locking. The full AQEC ($W_r = 1.45$ MHz, $W_b = 1.25$ MHz, $\nu_r = 0.8$ MHz, $\nu_b = -0.9$ MHz, $\Omega_1 = \Omega_2 = 0.39$ MHz) demonstrates further improvement from photon-loss correction. We plot the density matrices of the logical states after preparation and after 9 μ s in Appendix H for reference.

To demonstrate that our protocol corrects single-photon loss error, in Fig. 3, we plot the combined population of error states as a function of time for all three cases. The error populations are computed through the expectation values of $\varepsilon_0 = |ge\rangle\langle ge| + |eg\rangle\langle eg|$ for $|L_0\rangle$, $\varepsilon_1 = |ef\rangle\langle ef| + |fe\rangle\langle fe|$ for $|L_1\rangle$, and $\varepsilon_0 + \varepsilon_1$ for $|L_x\rangle$ corresponding to the states after single-photon loss. We extract the error population from the density matrices reconstructed with full two-qutrit state tomography at each time point up to 27 μ s using the Maximum Likelihood Estimation (MLE) from 5000 measurements for each state. This is a direct demonstration of the AQEC's effectiveness, as it measures the error state population designed to correct by the protocol. Compared to the free decay cases (black dots), turning on the AQEC clearly corrects photon loss and suppresses the error rate below the free decay cases (green dots). The error rates for all three logical states increase in the 4 QQ echo case (blue dots), as enhanced qutrit decay rates in the presence of sideband can lead to extra photon loss. The solid lines represent rotating frame simulations and are in agreement with the experimental data.

In addition to correcting photon loss, it is also important to characterize how well the AQEC protocol preserves the coherence of the logical states. To quantify the coherence, we plot the decay of the most sensitive off-diagonal matrix element for each logical state. Fitting the data to the exponential decays for $|L_0\rangle$ and

$|L_1\rangle$ [38], the logical states' coherence are improved from 11.8 μ s ($|L_0\rangle$) and 3.3 μ s ($|L_1\rangle$) in the free decay cases, to 18.6 μ s and 17.1 μ s in the four QQ echo cases, and up to 23.4 μ s and 16.9 μ s in the error correction cases (see Fig. 4(a), (b)). This demonstrates a factor of 2.0 and 5.1 improvement in logical state coherence against the free decay case. We use the operator $\tilde{X} = (|gg\rangle + |ff\rangle)(\langle gf| + \langle ff|)/2 + h.c.$ for showing $|L_x\rangle$'s coherence. \tilde{X} is the projection of the error-transparent logical X rotation $(I + X_1)X_2/2$ to the $\{|g\rangle, |f\rangle\}$ subspace, with $X_j = (a_{qj}^\dagger a_{qj}^\dagger + a_{qj} a_{qj})/\sqrt{2}$ [16]. In Fig. 4, the solid and dashed lines represent rotating-frame simulations and fit, matching qualitatively to the experimental data. Our results demonstrate a factor of 1.4 improvement in $|L_x\rangle$'s lifetime.

The large difference in free-decay coherence times between $|L_0\rangle$ and $|L_1\rangle$ originates from the low-frequency dephasing noise on Φ_{DC} through the flux line. It causes a shift in both transmons' frequencies in the same direction, which $|L_1\rangle$ is sensitive to but $|L_0\rangle$ is not. The passive echo protection from the Star code drives suppresses this; consequently, in the 4 QQ echo case both logical states have similar coherence time.

The AQEC performance is primarily limited by three factors in our experiment. The most important fact is that the QQ sideband rates W_r and W_b are well below their ideal values. Stronger drives would further suppress phase noise (lifetimes in the 4 QQ echo experiment are well below $2T_1$, indicating room for improvement), and the increased energy separation would also allow us to use stronger QR drives, correcting photon loss more quickly. Although the coupler supports 9 MHz QQ sidebands for short periods, when W_b goes beyond 5 MHz the readout resonator frequency starts to shift, introducing systematic measurement distortion (See Appendix E for details). This problem worsens with all six tones applied and we stay well below this limit to ensure reliable tomography results. The second limit is the ZZ coupling between the transmons, an extra dephasing channel for superposition states (see Appendix D for details). Our

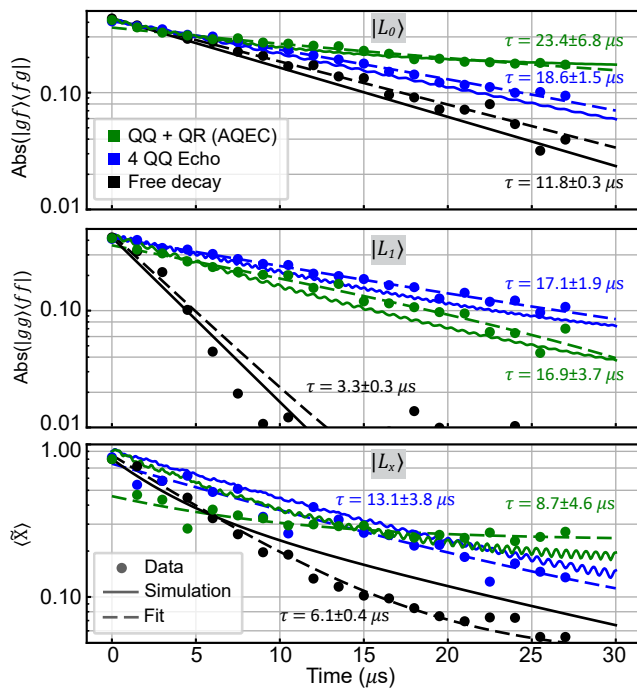


FIG. 4. Coherence improvement. Black, blue, and green circles are experimentally obtained expectation values for the relevant operators representing coherence at a given time. The expectation values are extracted from the tomographic reconstruction of states with 5000 repeated measurements. The improvement with AQEC turned on is explained by the master equation simulation. All traces are fitted to the exponential decay curve $A \exp(-t/\tau) + C$. The error bars (one standard deviation) for τ are obtained from the fitting*. The fast transition period (first $1.5 \mu\text{s} \sim \Omega_j^{-1}$ in the AQEC case is not included in the fitting for a better representation of logical coherence.

*Large error comes from treating C as a free variable in the fitting.

coupler is operated at the minimum ZZ flux bias of the coupler to minimize the effect. It could be further mitigated by stronger QR sidebands enabling faster error correction, or through additional off-resonant QQ drive terms to dynamically cancel it. The third limit comes from heating and physical coherence drop when sidebands are turned on. The average photon number in the readout increases from < 0.01 (free decay and 4 QQ echo cases) to 0.03 (AQEC case), and the photon-excitation event in the transmon is a non-correctable error source (see Appendix I). This explains why a clear reduction in correctable error rate does not result in a comparable increase in the logical lifetime. Further improvement can thus come from two paths—improving isolation between control signals or improving physical qubit coherence so that weaker drives can be more effective. Other limits are in the order of ms as shown in Appendix I and do not affect our results considerably.

IV. CONCLUSION AND OUTLOOK

We have experimentally demonstrated a hardware-efficient AQEC code, the Star code, that requires only two transmon-resonator pairs and a linear coupler to perform the second-order transitions. Three levels per transmon are used to store information, with the middle level capturing photon loss error, and entropy is dumped to the resonator autonomously through the always-on cooling sidebands. Inter-transmon parametric drives are applied to the coherence-preserving coupler for separating the Star code logical space. We demonstrate AQEC's effectiveness in a pure transmon system that is free from 3D cavities, compared to previous AQEC demonstrations in the bosonic system. Our system is entirely constructed from scalable components and fundamentally avoids the need for fast and accurate error detection and feedback error correction pulses. The Star code can be a self-corrected building block for the surface code [3, 39] to further correct higher-order errors when scaled up.

Future work will include realizing proposed error-transparent single-qubit and multi-qubit gates [16]. The Star code can also be implemented in other platforms that have full control of multiple anharmonic three-level systems.

V. ACKNOWLEDGEMENT

This work was supported by AFOSR Grant No. FA9550-19-1-0399 and ARO Grant No. W911NF-17-S0001. Devices are fabricated in the Pritzker Nanofabrication Facility at the University of Chicago, which receives support from Soft and Hybrid Nanotechnology Experimental (SHyNE) Resource (NSF ECCS-1542205), a node of the National Science Foundation's National Nanotechnology Coordinated Infrastructure. This work also made use of the shared facilities at the University of Chicago Materials Research Science and Engineering Center, supported by the National Science Foundation under award number DMR-2011854. EK's research was additionally supported by NSF Grant No. PHY-1653820.

Appendix A: Device Parameters

Transition	T_1 (μs)	T_R (μs)	T_{echo} (μs)
$Q_1 e\rangle \rightarrow g\rangle$	24.3	15.2	24.6
$Q_2 e\rangle \rightarrow g\rangle$	9.1	9.8	14.3
$Q_1 f\rangle \rightarrow e\rangle$	27.1	16.7	29.3
$Q_2 f\rangle \rightarrow e\rangle$	26.7	20.1	34.3
$R_1 1\rangle \rightarrow 0\rangle$	0.3		
$R_2 1\rangle \rightarrow 0\rangle$	0.3		

TABLE I. Device coherence parameters.

Relevant coherence parameters and frequencies at the operating point (Coupler DC flux bias $\Phi_{\text{DC}} = 0.3795\Phi_0$) without external drives are listed in Table. I and Table. II. The ZZ coupling (dispersive shifts) between two-transmon energy levels are measured in the experiment through Ramsey fringe frequency difference (Appendix G), and the cross-Kerr couplings J_{11} , J_{21} , J_{12} , J_{22} are calculated from the measurement results.

Appendix B: Star code frame transformation

We explicitly show the Hamiltonian for the Star code in different frames, with the sideband parameter set $\{W_r = W_b = W, \Omega_j = \Omega, \nu_r, \nu_b\}$. Without the external drives, the device can be described by the following Hamiltonian in the lab frame by keeping leading-order terms,

$$H = \sum_{j=1}^2 \left(\omega_{qj} n_{qj} + \frac{\alpha_j}{2} n_{qj} (n_{qj} - 1) + \omega_{rj} n_{rj} + \chi_j n_{qj} n_{rj} \right) + \sum_{j,k=1,2} J_{jk} (n_{q1})^j (n_{q2})^k. \quad (\text{B1})$$

Parameter	Symbol	Value/ 2π
Q_1 ge frequency	ω_{q1}	3.2049 GHz
Q_2 ge frequency	ω_{q2}	3.6625 GHz
Q_1 anharmonicity	α_1	-116.4 MHz
Q_2 anharmonicity	α_2	-159.6 MHz
R_1 frequency	ω_{r1}	4.9946 GHz
R_2 frequency	ω_{r2}	5.4505 GHz
R_1 dispersive shift	χ_1	-180 kHz
R_2 dispersive shift	χ_2	-330 kHz
$(E_{ ee\rangle} - E_{ ge\rangle}) - (E_{ eg\rangle} - E_{ gg\rangle})$	ZZ_{ge}	-261 kHz
$(E_{ fe\rangle} - E_{ ee\rangle}) - (E_{ fg\rangle} - E_{ eg\rangle})$	ZZ_{ef1}	-130 kHz
$(E_{ ef\rangle} - E_{ ee\rangle}) - (E_{ gf\rangle} - E_{ ge\rangle})$	ZZ_{ef2}	-301 kHz
$(E_{ ff\rangle} - E_{ ef\rangle}) - (E_{ fg\rangle} - E_{ eg\rangle})$	ZZ_{ff1}	-171 kHz
$(E_{ ff\rangle} - E_{ fe\rangle}) - (E_{ gf\rangle} - E_{ ge\rangle})$	ZZ_{ff2}	-289 kHz
$(E_{ ef\rangle} - E_{ gf\rangle}) - (E_{ eg\rangle} - E_{ gg\rangle})$	ZZ_{gf1}	-619 kHz
$(E_{ fe\rangle} - E_{ fg\rangle}) - (E_{ ge\rangle} - E_{ gg\rangle})$	ZZ_{gf2}	-464 kHz
Coefficient of $n_{q1}n_{q2}$	J_{11}	-312 kHz
Coefficient of $n_{q1}^2n_{q2}$	J_{21}	25 kHz
Coefficient of $n_{q1}n_{q2}^2$	J_{12}	-49 kHz
Coefficient of $n_{q1}^2n_{q2}^2$	J_{22}	-43 kHz

TABLE II. Device frequencies without external drives.

Capacitance (fF)	Josephson Energy (GHz)		
C_{q1}	165.9	E_{j1}	12.4
C_{q2}	123.4	E_{j2}	12.1
C_c	178.3	E_{jc}	1106.0
C_{q12}	2.0		

TABLE III. Capacitances and Josephson energies used in the simulation. Capacitances are extracted through design geometry simulations in ANSYS Q3D, and Josephson energies are calculated from the room temperature resistances of identical test junctions on the same chip.

Here $n_{qj} = a_{qj}^\dagger a_{qj}$ and $n_{rj} = a_{rj}^\dagger a_{rj}$ are the photon number operators for the j -th transmon and resonator respectively with $a_{qj(rj)}$ representing the annihilation operator for the j -th transmon (resonator). χ_j and J_{jk} are the ZZ coupling strength between the j -th QR pair and between two transmons. Inter-transmon ZZ couplings are expanded to the second order for explaining shifts up to $|f\rangle$ level. Cross-Kerr couplings J_{jk} are minimized by biasing DC flux at $\Phi_{\text{DC}} = 0.3795\Phi_0$ to suppress logical states' extra dephasing channel (see derivation in Appendix D).

Then we bring in external drives and ignore the static ZZ couplings between QQ and QR, which can be reintroduced into the equation by shifting the diagonal energies. The *lab-frame* Hamiltonian then reads

$$H_{\text{lab}} = \sum_{j=1,2} \left(\omega_{qj} a_{qj}^\dagger a_{qj} + \frac{\alpha_j}{2} a_{qj}^\dagger a_{qj}^\dagger a_{qj} a_{qj} + \omega_{rj} a_{rj}^\dagger a_{rj} \right) + H_{QQ} + H_{QR1} + H_{QR2}, \quad (\text{B2})$$

$$H_{QQ} = A_{QQ}(t) \left(a_{q1}^\dagger + a_{q1} \right) \left(a_{q2}^\dagger + a_{q2} \right),$$

$$H_{QRj} = A_{QRj}(t) \left(a_{qj}^\dagger + a_{qj} \right) \left(a_{rj}^\dagger + a_{rj} \right),$$

$$A_{QQ}(t) = \frac{W}{\sqrt{2}} \cos((\omega_{q2} - \omega_{q1} - \alpha_1 - \nu_r)t) + \frac{W}{\sqrt{2}} \cos((\omega_{q2} - \omega_{q1} + \alpha_2 + \nu_r)t) + W \cos((\omega_{q1} + \omega_{q2} - \nu_b)t) + \frac{W}{2} \cos((\omega_{q1} + \omega_{q2} + \alpha_1 + \alpha_2 + \nu_b)t),$$

$$A_{QRj}(t) = \frac{\Omega}{\sqrt{2}} \cos((\omega_{qj} + \omega_{rj} + \alpha_j)t).$$

Next, we move to the “*logical-static*” frame where all logical states have zero energy resulting in (we keep the

lowest two levels for the resonators)

$$\begin{aligned}
\tilde{H}_{\text{static}} &= -\frac{\alpha_1}{2}(P_{eg} + P_{ef}) - \frac{\alpha_2}{2}(P_{ge} + P_{fe}) \\
&\quad + \tilde{H}_{QQ} \\
&\quad - \sum_{j=1,2} \frac{\alpha_j}{2} a_{rj}^\dagger a_{rj} + \tilde{H}_{QRj}, \quad (\text{B3}) \\
\tilde{H}_{QQ} &= \frac{W}{2} (|ee\rangle \langle gf| e^{2\pi i \nu_r t} + |ee\rangle \langle fg| e^{2\pi i \nu_r t} \\
&\quad + |ee\rangle \langle gg| e^{2\pi i \nu_b t} + |ee\rangle \langle ff| e^{2\pi i \nu_b t}) \otimes I_4 \\
&\quad + h.c., \\
\tilde{H}_{QR1} &= \frac{\Omega}{2} (|eg\rangle \langle fg| + |ef\rangle \langle ff|) \otimes |0\rangle \langle 1| \otimes I_2 + h.c., \\
\tilde{H}_{QR2} &= \frac{\Omega}{2} (|ge\rangle \langle gf| + |fe\rangle \langle ff|) \otimes I_2 \otimes |0\rangle \langle 1| + h.c..
\end{aligned}$$

Finally, we perform another rotating frame transformation so that the detuned QQ sidebands become time-independent, which leads to

$$\begin{aligned}
\tilde{H}_{\text{rot}} &= -\frac{\alpha_1}{2}(P_{eg} + P_{ef}) - \frac{\alpha_2}{2}(P_{ge} + P_{fe}) \\
&\quad - \nu_r(P_{gf} + P_{fg} + P_{ge} + P_{eg}) \\
&\quad - \nu_b(P_{gg} + P_{ff} + P_{ef} + P_{fe}) \\
&\quad + \tilde{H}'_{QQ} \\
&\quad - \sum_{j=1,2} \frac{\alpha_j}{2} a_{rj}^\dagger a_{rj} + \tilde{H}_{QRj}, \quad (\text{B4}) \\
\tilde{H}'_{QQ} &= \frac{W}{2} (|ee\rangle \langle gf| + |ee\rangle \langle fg| \\
&\quad + |ee\rangle \langle gg| + |ee\rangle \langle ff| + h.c.) \otimes I_4.
\end{aligned}$$

Here I_n is the $n \times n$ identity matrix and $P_{ab} = |ab\rangle \langle ab| \otimes I_4$. Rotating Wave Approximation (RWA) is applied in the last two transformations. In the final frame, $\{|L_0\rangle, |L_1\rangle\}$ have different energies $\{-\nu_r, -\nu_b\}$, and the superposition states become time-dependent.

Appendix C: Circuit Hamiltonian and sideband strength

Fig. 5a is our device's false color optical picture. We first consider the Hamiltonian of the two transmons:

$$\begin{aligned}
H_Q &= \vec{n}^\top C_L^{-1} \vec{n} - E_{j1} \cos(\varphi_c - \varphi_1) - E_{j2} \cos(\varphi_2 - \varphi_c) \\
&\quad - E_{jc} \cos\left(\pi \frac{\Phi_{\text{ext}}}{\Phi_0}\right) \cos(\varphi_c), \quad (\text{C1a})
\end{aligned}$$

$$C_L = \begin{bmatrix} C_{q1} + C_{q12} & -C_{q12} & 0 \\ -C_{q12} & C_{q2} + C_{q12} & 0 \\ 0 & 0 & C_{q1} + C_{q2} + C_{qc} \end{bmatrix}, \quad (\text{C1b})$$

$$\vec{n}^\top = (n_1, n_2, n_c), \quad [n_j, \varphi_j] = -i. \quad (\text{C1c})$$

Here \vec{n} and $\vec{\varphi}$ are the charge and phase variables and can be found through the Legendre transformation. Table. III includes all coefficients used in the quantization.

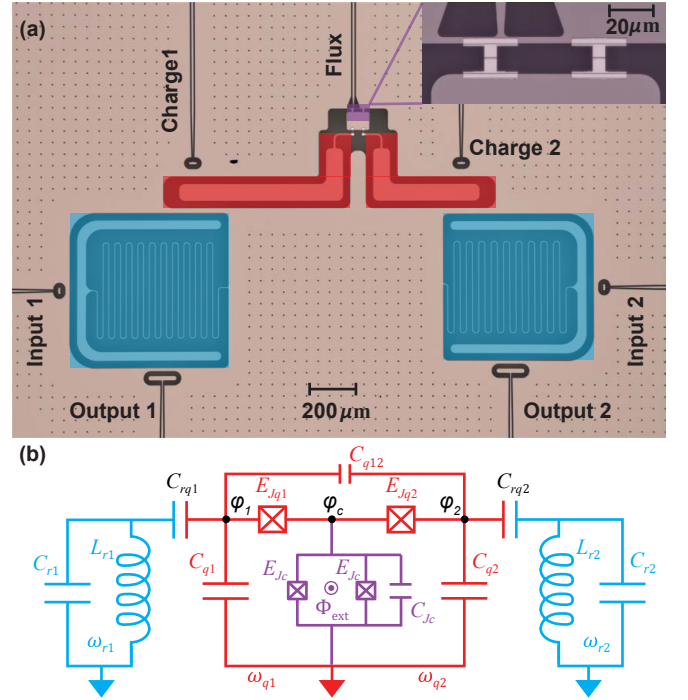


FIG. 5. The device. (a) False-colored optical image. Two transmons (red) are inductively connected through a SQUID loop (purple, inset shows zoomed-in image). An on-chip flux line is coupled to the SQUID for activating QQ sidebands through parametric RF flux modulation at the proper DC flux position. Each transmon is capacitively coupled to the readout resonator (blue). Single transmon pulses are sent through the resonator input lines. QR sidebands are applied through corresponding charge lines. (b) Circuit schematic diagram.

Then we extract the linear part of H_Q to obtain

$$\begin{aligned}
H_0 &= \vec{n}^\top C_L^{-1} \vec{n} + \frac{E_{j1}}{2} (\varphi_c - \varphi_1)^2 + \frac{E_{j2}}{2} (\varphi_2 - \varphi_c)^2 \\
&\quad + \frac{E_{jc}}{2} \cos\left(\pi \frac{\Phi_{\text{ext}}}{\Phi_0}\right) \varphi_c^2. \quad (\text{C2})
\end{aligned}$$

Next, we rewrite the charge and phase variables in the dressed basis with the unitary transformation matrix U such that H_0 is simultaneously diagonalized to find out the normal modes,

$$H_0 = \sum_{j=1,2,c} \left(\tilde{C}_j \tilde{n}_j^2 + \tilde{D}_j \tilde{\varphi}_j^2 \right), \quad (\text{C3a})$$

$$\vec{n} = (\tilde{n}_1, \tilde{n}_2, \tilde{n}_c)^\top = U^{-1} \vec{n}, \quad (\text{C3b})$$

$$\vec{\varphi} = (\tilde{\varphi}_1, \tilde{\varphi}_2, \tilde{\varphi}_c)^\top = U^{-1} \vec{\varphi}, \quad (\text{C3c})$$

$$U = \begin{bmatrix} U_{11} & U_{12} & U_{1c} \\ U_{21} & U_{22} & U_{2c} \\ U_{c1} & U_{c2} & U_{cc} \end{bmatrix}. \quad (\text{C3d})$$

In the dressed basis, the nonlinear part is reintroduced

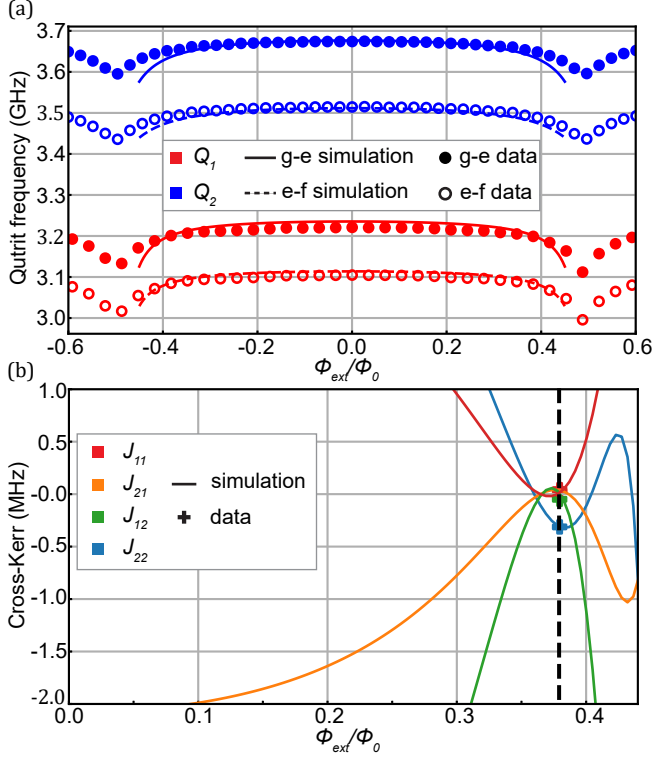


FIG. 6. Circuit quantization results of H_Q . Comparison of (a) transmon frequencies and (b) cross-Kerr couplings between simulation and experiment. Q_1 (red) and Q_2 's (blue) $|g\rangle \leftrightarrow |e\rangle$ and $|e\rangle \leftrightarrow |f\rangle$ frequencies from numerical calculation and experiment are plotted as a function of Φ_{ext} . Four inter-quitrit cross-Kerr coupling strengths, J_{11} , J_{21} , J_{12} and J_{22} are calculated, and experiment data are marked out on the Star code operating point (dashed line).

in the Hamiltonian to get

$$\begin{aligned}
 H_Q = & \sum_{j=1,2,c} \left(\tilde{C}_j \tilde{n}_j^2 \right) \\
 & - E_{j1} \cos \left(\sum_{j=1,2,c} (U_{cj} \tilde{\varphi}_j - U_{1j} \tilde{\varphi}_j) \right) \\
 & - E_{j2} \cos \left(\sum_{j=1,2,c} (U_{2j} \tilde{\varphi}_j - U_{cj} \tilde{\varphi}_j) \right) \\
 & - E_{jc} \cos \left(\pi \frac{\Phi_{\text{ext}}}{\Phi_0} \right) \cos \left(\sum_{j=1,2,c} U_{cj} \tilde{\varphi}_j \right), \quad (\text{C4a})
 \end{aligned}$$

with

$$\tilde{n}_j = \frac{i}{\sqrt{2}} \sqrt{\frac{\tilde{D}_j}{\tilde{C}_j}} \left(a_{qj}^\dagger - a_{qj} \right), \quad (\text{C4b})$$

$$\tilde{\varphi}_j = \frac{1}{\sqrt{2}} \sqrt{\frac{\tilde{C}_j}{\tilde{D}_j}} \left(a_{qj}^\dagger + a_{qj} \right). \quad (\text{C4c})$$

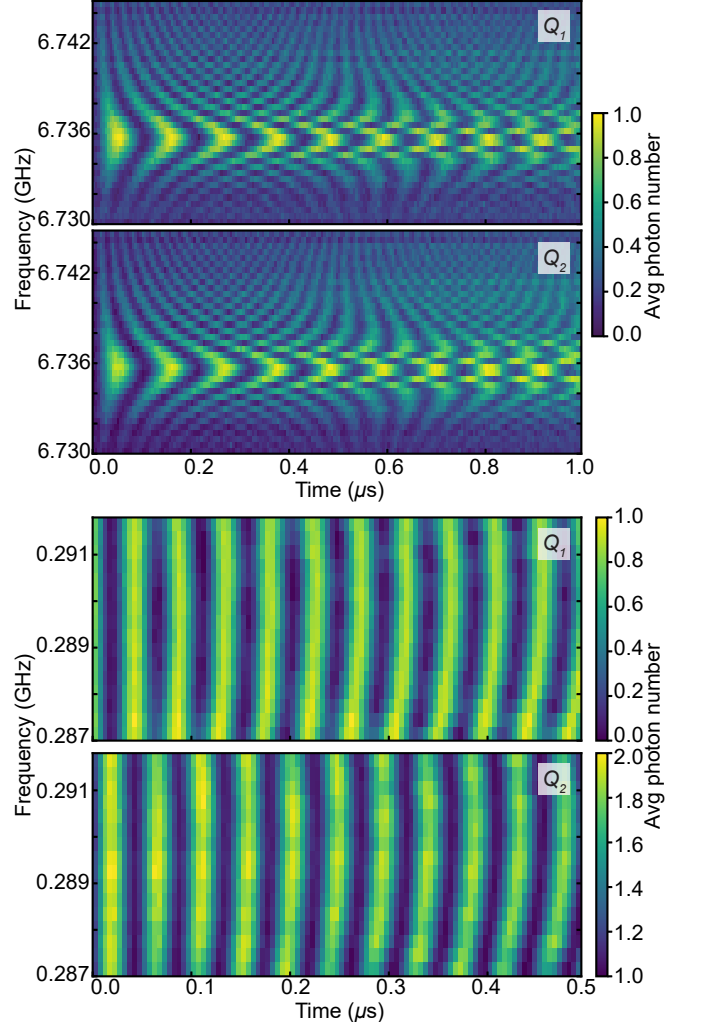


FIG. 7. Chevron plots for fast QQ sidebands. The state of both transmons are simultaneously read out and shown as photon numbers. Top two figures show 9 MHz $|gg\rangle \leftrightarrow |ee\rangle$, and bottom two demonstrate 21 MHz $|ee\rangle \leftrightarrow |gf\rangle$ oscillations.

We use the scQubits package [40] to quantize the Hamiltonian. The numeric and experiment comparison are shown in Fig. 6. When Φ_{ext} is biased close to $\Phi_0/2$, deviation appeared in numerics. This comes from the asymmetry of SQUID junctions' resistances and parasitic SQUID loop inductance and is away from our bias point. Around the DC flux position where the Star code protocol is implemented (marked as Fig. 6b dash line), we have a decent explanation of both transmons' frequencies and cross-Kerr couplings.

The QQ sidebands are realized through parametric RF flux modulation of the coupler. To understand the sideband rate, we follow the previous paper [34] and apply an adiabatic approximation to the Hamiltonian: The coupler mode frequency remains high (> 15 GHz) above transmons' frequencies (< 4 GHz) in the system, therefore the coupler can be assumed static at the ground state. The non-dynamical potential of the coupler mode

is removed by minimizing the Hamiltonian. Transmons are treated as duffing oscillators when calculating the effective sideband rate. Keeping up to 2nd order expansions, the Hamiltonian H_{ad} under adiabatic approximation is

$$\begin{aligned} H_{ad} &= \omega_{q1} a_{q1}^\dagger a_{q1} + \omega_{q2} a_{q2}^\dagger a_{q2} \\ &+ \frac{\alpha_1}{2} a_{q1}^\dagger a_{q1}^\dagger a_{q1} a_{q1} + \frac{\alpha_2}{2} a_{q2}^\dagger a_{q2}^\dagger a_{q2} a_{q2} \\ &+ g_1(t) (a_{q1}^\dagger + a_{q1}) (a_{q2}^\dagger + a_{q2}) \\ &+ g_2 (-a_{q1}^\dagger + a_{q1}) (-a_{q2}^\dagger + a_{q2}), \end{aligned} \quad (\text{C5a})$$

$$g_1(t) = \frac{\sqrt{E_{j1} E_{j2}}}{2E_{jc} \cos\left(\pi \frac{\Phi_{\text{ext}}(t)}{\Phi_0}\right)} \sqrt{\omega_{q1} \omega_{q2}}, \quad (\text{C5b})$$

$$g_2 = \frac{\sqrt{C_{q1} C_{q2}}}{2C_{q12}} \sqrt{\omega_{q1} \omega_{q2}}. \quad (\text{C5c})$$

Here $g_1(t)$ and g_2 are flux-tunable inductive coupling strength and constant capacitive coupling strength. Plugging in the RF flux modulation $\frac{\pi \Phi_{\text{ext}}(t)}{\Phi_0} = \Phi_{\text{DC}} + \epsilon \cos(\omega_d t)$ into Eq. C5b and assuming $\epsilon \ll \Phi_{\text{DC}}$, we obtain

$$\begin{aligned} g_1(t) &= \frac{\sqrt{E_{j1} E_{j2}}}{2E_{jc}} \sqrt{\omega_{q1} \omega_{q2}} \frac{1}{\cos(\Phi_{\text{DC}} + \epsilon \cos(\omega_d t))} \\ &= \frac{\sqrt{E_{j1} E_{j2}}}{2E_{jc}} \sqrt{\omega_{q1} \omega_{q2}} \frac{(1 + \epsilon \sin(\omega_d t) \tan(\Phi_{\text{DC}}))}{\cos(\Phi_{\text{DC}})}. \end{aligned} \quad (\text{C6})$$

Therefore the QQ sideband rate becomes (suppose $|\psi_1\rangle$ and $|\psi_2\rangle$ are states connected by the sideband)

$$\frac{\sqrt{E_{j1} E_{j2}}}{2E_{jc}} \sqrt{\omega_{q1} \omega_{q2}} \frac{\epsilon \tan(\Phi_{\text{DC}})}{\cos(\Phi_{\text{DC}})} A_{12}, \quad (\text{C7})$$

with

$$A_{12} = \langle \psi_1 | (a_{q1}^\dagger + a_{q1}) (a_{q2}^\dagger + a_{q2}) | \psi_2 \rangle,$$

and is proportional to the flux modulation rate. A_{12} is the state-dependent bosonic enhancement coefficient. Higher order corrections can be calculated using time-dependent Schrieffer–Wolff transformation[41], and for our inductive coupler, both QQ blue and red sideband will have a similar rate under the same ϵ .

Each transmon is capacitively coupled to the readout resonator, and the second-order QR error-correcting sidebands are generated through the charge drive at half the transition energy $\omega_{dqrj} = (\omega_{qj} + \omega_{rj} + \alpha_{qj})/2$ with drive amplitude ϵ_{qj} ,

$$\begin{aligned} H_{QRj} &= \omega_{qj} a_{qj}^\dagger a_{qj} + \frac{\alpha_j}{2} (a_{qj}^\dagger)^2 (a_{qj})^2 + \omega_{rj} a_{rj}^\dagger a_{rj} \\ &+ g_{qrj} (-a_{qj}^\dagger + a_{qj}) (-a_{rj}^\dagger + a_{rj}) \\ &+ \epsilon_{qj} (a_{qj}^\dagger e^{-i\omega_{dqrj} t} + h.c.). \end{aligned} \quad (\text{C8})$$

The effective QR sideband rate is $\Omega_j = 16g_{qrj}^3 \epsilon_{qj}^2 / (\omega_{qj} - \omega_{rj})^4$ [35]. Under the same Purcell limit ($\sim \frac{g_{qrj}^2 \kappa_j}{(\omega_{qj} - \omega_{rj})^2}$) from the resonator, smaller QR frequency difference allows higher QR sideband rate for the same drive amplitude. In our experiment, the Purcell limit from the resonator is larger than 200 μs , and is not limiting the physical coherence time.

Appendix D: Transmon ZZ induced dephasing

Realizing AQEC requires error transparency to single photon loss error. This makes ZZ coupling an extra logical dephasing channel as it does not commute with \tilde{H}_{star} . In a two qutrit system, there are in total 7 different ZZ frequency shifts coming from 4 cross-Kerr coupling strengths $J_{11}, J_{21}, J_{12}, J_{22}$. However, not all ZZ couplings are detrimental to the Star code. The error transparency requires no phase accumulation between logical states during the error correction process. This is equivalent to having the same energy for the photon lost from one transmon, independent of the state of the partner transmon,

$$\begin{aligned} E_{ff} - E_{ef} &= E_{fg} - E_{eg}, \\ E_{ff} - E_{fe} &= E_{gf} - E_{ge}. \end{aligned} \quad (\text{D1})$$

Here E_{jk} refers to the energy of the state $|jk\rangle$. Equations D1 are equivalent to $ZZ_{ff2} = ZZ_{ff1} = 0$ (see Table II). When this is not the case, a random phase difference will accumulate between logical states after the error correction, introducing dephasing to the logical superposition states. The other ZZs are naturally error transparent in the logical manifold since $|ee\rangle$ is dark and will not affect the logical states' coherence. To suppress the ZZ-induced logical dephasing, we can increase the QR sideband rate Ω_j , shortening the $|e\rangle$ population time in both qutrits and reducing the accumulated random logical phase. To eliminate this dephasing channel, we need a coupler that has zero ZZ_{ff1} and ZZ_{ff2} when all external sidebands are turned on. This can be potentially realized in our current coupler with dispersive shift engineering. We consider a two-transmon system with static interaction that produces a set of dispersive shifts for cancellation. The base Hamiltonian H_{base} is

$$\begin{aligned} H_{\text{base}} &= \sum_n (\epsilon_{1,n} |n_1\rangle \langle n_1| + \epsilon_{2,n} |n_2\rangle \langle n_2|) \\ &+ \sum_{nm} \Delta_{nm} |n_1 m_2\rangle \langle n_2 m_1|, \end{aligned} \quad (\text{D2})$$

where $\epsilon_{1/2,n}$ are energies for single transmon levels, Δ_{nm} is the static energy shift to the state when transmon 1 has n photons and transmon 2 has m photons. For the ground state $\epsilon_{1/2,0}$ and Δ_{00} are set to 0. We add to H_{base} a QQ red sideband through the coupler,

$$H_D = 2g \sin(2\pi\nu t) (a_{q1}^\dagger a_{q2} + a_{q1} a_{q2}^\dagger). \quad (\text{D3})$$

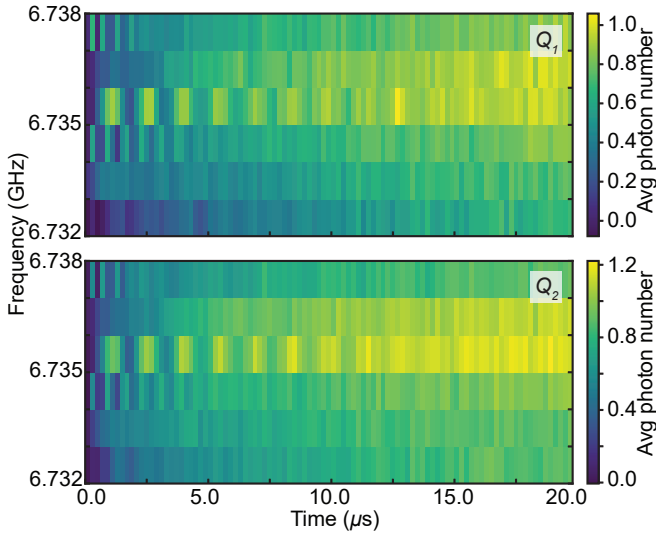


FIG. 8. Readout saturation feature for fast (rate 9 MHz) QQ blue sideband $|gg\rangle \leftrightarrow |ee\rangle$ in the long time scale. Top and bottom panel show readout signals from the first and second resonators.

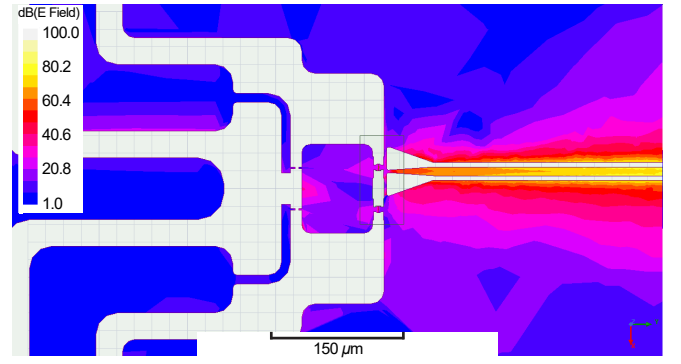
We assume the frequency detuning ν is far off-resonant so that $\nu \gg g$, and this will introduce an energy shift D_{jk} to all levels:

$$D_{jk}^{(R)} = \frac{g^2 j(k+1)}{E_{j,k} - E_{j-1,k+1} - \nu} + \frac{g^2 j(k+1)}{E_{j,k} - E_{j-1,k+1} + \nu} + \frac{g^2 (j+1)k}{E_{j,k} - E_{j+1,k-1} - \nu} + \frac{g^2 (j+1)k}{E_{j,k} - E_{j+1,k-1} + \nu}. \quad (\text{D4})$$

For a detuned QQ blue sideband drive, one can find a similar expression for the energy shift,

$$D_{jk}^{(B)} = \frac{g^2 (j+1)(k+1)}{E_{j,k} - E_{j+1,k+1} - \nu} + \frac{g^2 (j+1)(k+1)}{E_{j,k} - E_{j+1,k+1} + \nu} + \frac{g^2 jk}{E_{j,k} - E_{j-1,k-1} - \nu} + \frac{g^2 jk}{E_{j,k} - E_{j-1,k-1} + \nu}. \quad (\text{D5})$$

When multiple external QQ sidebands are applied, the total dispersive shift to each energy level is given by $D_{jk} = \sum D_{jk}^{(R)} + \sum D_{jk}^{(B)}$, where the sum is over all external QQ sidebands. Specifically for the Star code scheme, we can modulate two extra QQ sidebands near $|ef\rangle \leftrightarrow |gh\rangle$ and $|fe\rangle \leftrightarrow |hg\rangle$. This can introduce either positive or negative D_{12} and D_{21} to the system, depending on the choices of frequency detuning. The required g for complete ZZ cancellation can be less than 5 MHz. Therefore, it is theoretically possible to cancel ZZ_{ff1} and ZZ_{ff2} simultaneously under such two extra drives. We did not turn on the cancellation sidebands in the experiment, because our readout suffers from frequency shift under strong flux modulation amplitude as discussed in Appendix E.



(a) RF flux modulation at 0.7 GHz

(b) RF flux modulation at 7 GHz

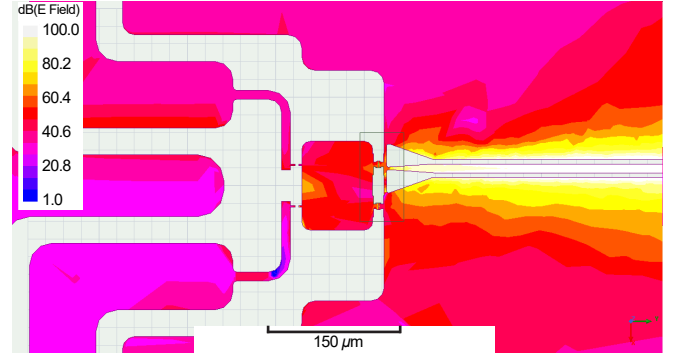


FIG. 9. Distribution of electrical field's amplitude (in log scale) when RF flux drive is modulated at (a) 700 MHz and (b) 7 GHz obtained from HFSS simulation.

Appendix E: Readout saturation and flux line optimization

In our device, we use the on-chip flux line to generate various two-qubit interactions through parametric modulation. A typical parametric coupler design includes two qubits capacitively or inductively coupled through a tunable coupler. Modulation of the coupler frequency and the qubit-coupler coupling strength contribute to the two-qubit interaction strength. For a capacitively coupled system [41–44], coupler frequency modulation contributes dominantly to the QQ sideband rate, and time-dependent Schrieffer-Wolff transformation (SWT) proves that [41] the ratio of interaction strengths between bswap and iswap is $\frac{\omega_1 - \omega_2}{\omega_1 + \omega_2}$ (ω_j is Q_j 's frequency). Therefore, a capacitive coupler provides a slower bswap than the iswap. In contrast, an inductively coupled system [34, 45] modulates the coupling strength between the qubit and coupler more effectively, and both iswap and bswap will have the same zeroth-order terms in the SWT expansion, thus theoretically sharing the same rate under same modulation amplitude. Previous experiments achieved fast iswap interactions, but a similar bswap rate has not been demonstrated in either type of parametric coupler yet. We experimentally realize a comparable maximum rates of 9 MHz bswap and 21 MHz iswap (shown in Fig. 7).

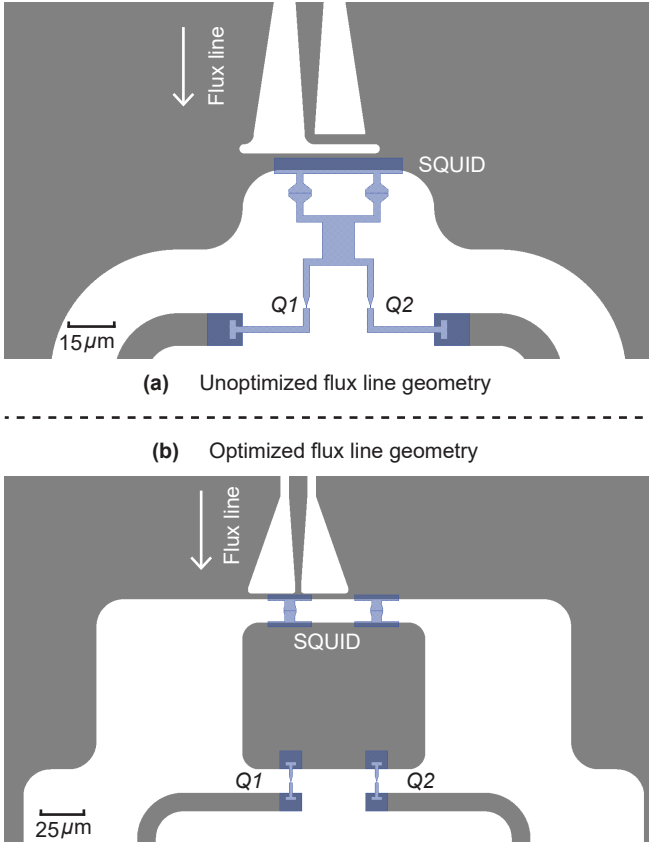


FIG. 10. SQUID design. (a) Old design without optimization. (b) Current design by maximizing the mutual inductance between the flux line and SQUID. The Ta and Al areas are colored as grey and blue separately, and the bare sapphire is colored white.

In the experiment, we notice that turning a strong bswap on will shift both resonators' frequencies after a long time, resulting in the 'saturation' feature (Fig. 8). Such a readout frequency shift is both sideband strength and duration dependent, and the shift persists for a noticeable period after all sidebands are turned off. Distinguishing transmons' states through readout becomes difficult when this happens. A readout is possible when the shift is reversed after waiting for a sufficiently long period but degrades readout fidelity due to transmons' relaxation. While case-dependent dynamic demarcation can distinguish states, this method becomes complex and inaccurate. In our experiment, we decided to lower the RF modulation amplitude and minimize the saturation region by optimizing the flux line geometry.

One source for the readout saturation at the bswap drive frequency is the flux line's stray charge coupling to the SQUID [45]. The on-chip flux line can be considered an antenna. The coupler is located in the near-field region, and the electrical field amplitude is proportional to the flux modulation frequency. Since bswap's drive frequencies are normally a magnitude higher than that of the iswap operations, a much stronger stray-charge drive

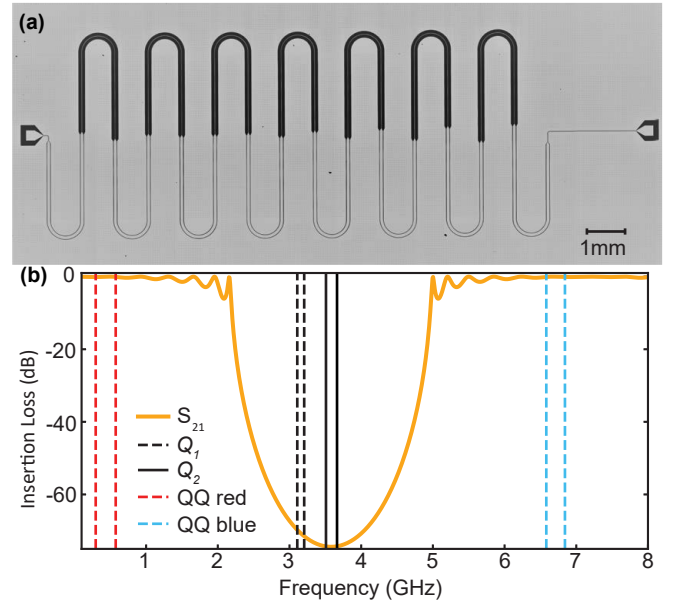


FIG. 11. The stepped impedance Purcell filter. (a) Optical image of our SIPF chip made using Ta on sapphire. (b) Calculated SIPF insertion loss. Transmon transitions, QQ red and blue sideband frequencies are marked in the plot.

is observed when the bswap drive is on.

We verify this fact using ANSYS HFSS simulation (see Fig. 9), where the electrical field amplitude is observed to increase over an order of magnitude when the modulation frequency is increased by a factor of 10. The stray charge drive limits the maximum power we can use for the flux modulation, and we focus on geometrical optimization to improve the flux-to-charge drive ratio. In order to do so, we maximize the mutual inductance between the SQUID and the flux line by increasing the SQUID loop size and bringing the flux line closer to the loop. The loop size in our experiment is limited by the SQUID's hysteresis [46] set by the ratio $\frac{L_{loop}}{L_{jc}}$, where L_{jc} is the inductance of each junction in the SQUID (assumed identical) and L_{loop} is the SQUID loop inductance. When $\frac{L_{loop}}{L_{jc}} > 1$, transmon frequencies become hysteric as a function of Φ_{DC} , and the region grows with the ratio. Dissipation appears when modulating within the hysteric region and should be avoided in our experiment. This property sets an upper bound for SQUID loop length.

We use HFSS simulation to calculate flux threaded by the SQUID loop and vary the geometry to maximize. Assuming the electrical field is geometry insensitive around the SQUID, maximizing SQUID flux increases the ratio between the mutual inductive coupling and stray capacitive coupling strength of the flux line. The original and optimized designs are shown in Fig. 10. The simulation suggests a factor of 3.5 improvement in the ratio.

Being strongly coupled to the SQUID, the flux line is also a channel for transmons' relaxation. In order to improve Purcell protection, we design a Stepped-Impedance

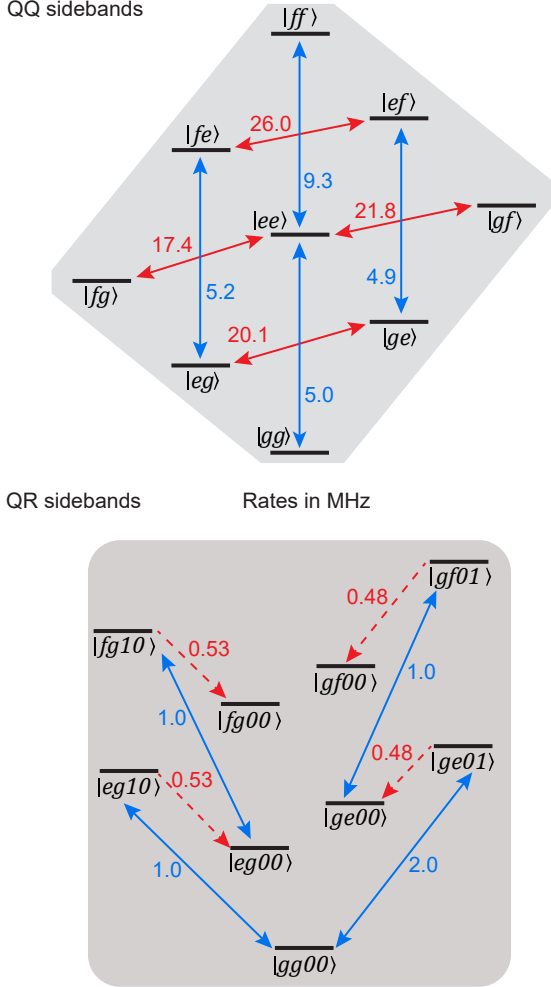


FIG. 12. QQ (top panel) and QR (bottom panel) sidebands with rates achieved in the experiment without readout saturation.

band-stop Purcell Filter (SIPF) as shown in Fig. 11, which strongly blocks transmon frequencies while allowing the QQ red and blue sideband drives to pass (see Fig. 21 for the full measurement setup).

Appendix F: QQ and QR sideband rates

The ability to sustain fast QQ sidebands is crucial to the realization of the Star code and we optimize the geometry of the device as discussed in the previous section. In Fig. 12(a), we show all two-photon QQ sidebands achieved in the experiment. Fig. 12(b) shows all experimentally achieved QR sidebands and resonator decay rates. The strong and rich two-photon processes with this design also show the potential of realizing high-fidelity two-qutrit gates [47].

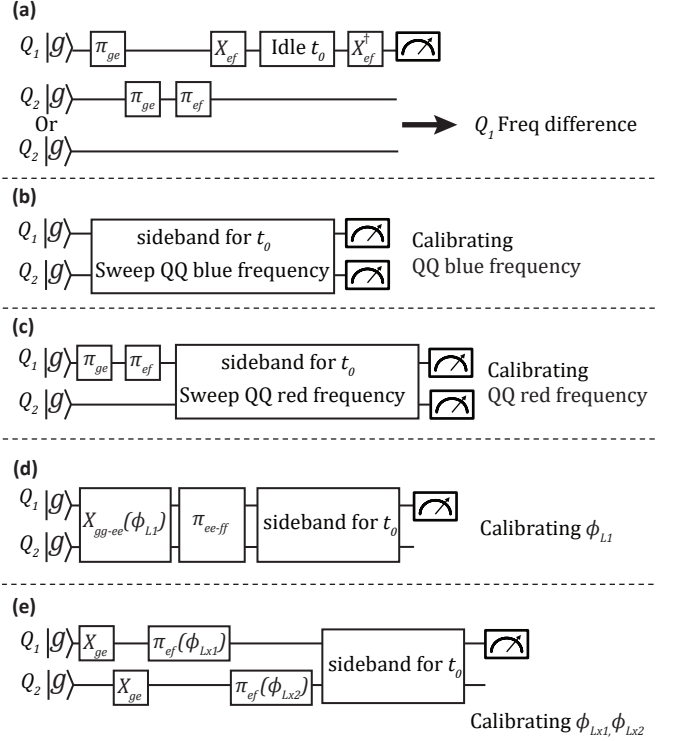


FIG. 13. Gate circuits for the Star code calibration. (a) Pulse sequence for calibration of ZZ_{ff1} . Ramsey-like protocol is used for the partner transmon being in $|g\rangle$ or $|f\rangle$. The other ZZ s are calibrated similarly. (b) QQ blue and (c) QQ red sideband frequency calibration sequence. QQ sideband pair frequencies are iteratively swept and updated based on the time-domain pattern. (d) $|L_1\rangle$ preparation phase calibration sequence. The phase point that has minimum $|e\rangle$ population in the sweep is chosen as the calibrated ϕ_{L1} . The preparation phase for $|L_0\rangle$ is calibrated similarly. (e) $|L_x\rangle$ preparation phase calibration protocol.

Appendix G: Full Star code calibration process

To implement the Star code, we need to calibrate the QQ and QR sideband frequencies when all sidebands are simultaneously on. The presence of external sidebands will change both transmons' frequencies through AC-stark shift and rectifying effect (RF modulation under a nonlinear frequency-flux response). In the experiment, we systematically perform the calibration, shown in Fig. 13.

In Fig. 13a, the static ZZ dispersive shift is characterized by measuring the Ramsey fringe frequency difference depending on the other qubit's state. In steps Fig. 13b and Fig. 13c, we first turn on all 6 QQ and QR drives at their bare frequencies. All QQ sideband rates are set to W when independently turned on. Two QQ red sidebands and two QQ blue sidebands are pair-swept separately as the 'red/blue pair'. The pair width and center are the sidebands' frequency difference and average. In each iteration step, we update sequentially the red and

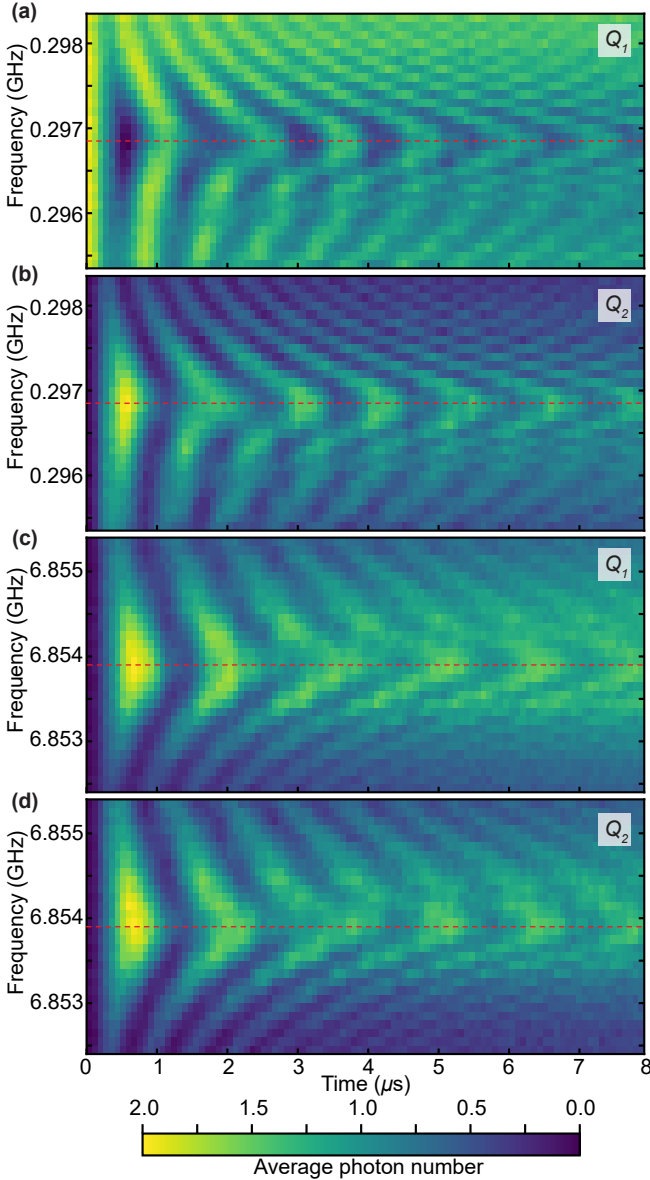


FIG. 14. Simultaneous QQ sideband calibration. All six tones used in the Star code are simultaneously turned on during the frequency-time sweep. The red (top two panels) and blue (bottom two panels) QQ sideband pair frequencies are swept individually for calibration in the presence of the other pair. Red dash lines in the plots represent the pairs' center frequency choices. (a) and (b) are Q_1 and Q_2 's average photon number when sweeping the red pair with the initial state $|fg\rangle$. (c) and (d) are Q_1 and Q_2 's average photon number when sweeping the blue pair with the initial state $|gg\rangle$.

blue pair centers, and the QR sideband frequencies. For each pair, we sweep the center frequency as a function of time with all six sidebands on. We use $|gg\rangle$ (blue pair) and $|fg\rangle$ (red pair) as the initial states. Reading out the average photon number in both transmons, the 2D sweep plots show a fringed chevron pattern (shown in Fig. 14). The pattern's center line is the new pair center.

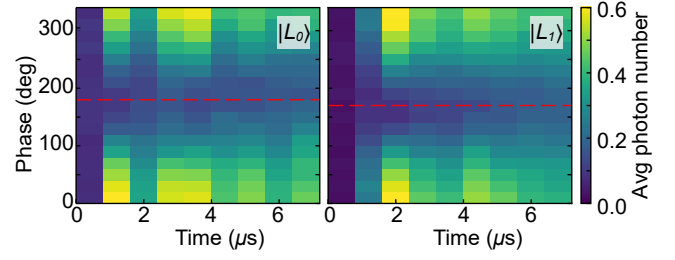


FIG. 15. Preparation phase calibration of $|L_0\rangle$ (left) and $|L_1\rangle$ (right) in the error correction experiment. The population of $|e\rangle$ on Q_1 are measured after turning on all sidebands for up to $8\mu\text{s}$, and the red dash line marks the calibrated phase position. We choose Q_1 due to higher readout fidelity.

The fringe rate represents the actual sideband detunings $\nu_{b/r}$ and rate $W_{b/r}$, and the detunings can be updated by changing pair width at this stage. After extracting both pairs' new centers, the QR sidebands are calibrated with $|eg\rangle$ and $|ge\rangle$ as the initial state when all drives are on. Populating $|f\rangle$ with the $|e0\rangle \leftrightarrow |f1\rangle$ process is most efficient when QR sidebands are on resonance. Because of non zero ZZ_{ff1} and ZZ_{ff2} , the QR sidebands cannot be exactly on resonance for both $|L_i\rangle$. In the experiment, we calibrate QR sidebands to be on resonance for the $|L_0\rangle$. For $|L_1\rangle$, the error correction process will be slower but not dephase the state after correction. After a few iterations, we get decent frequency calibrations of all six sidebands.

Logical state preparation includes both charge and flux drives with appropriate relative phases. Fig. 13d is to calibrate $|L_0\rangle$ and $|L_1\rangle$'s preparation phase. For the logical state $|L_0\rangle$, we first apply two π_{ge} pulses sequentially on Q_1 and Q_2 to prepare $|ee\rangle$ through charge lines. Afterwards a $(\pi/2)_{|ee\rangle \leftrightarrow |fg\rangle}$ pulse with a phase offset ϕ_{L0} and a $\pi_{|ee\rangle \leftrightarrow |fg\rangle}$ pulse are applied through the flux line. To

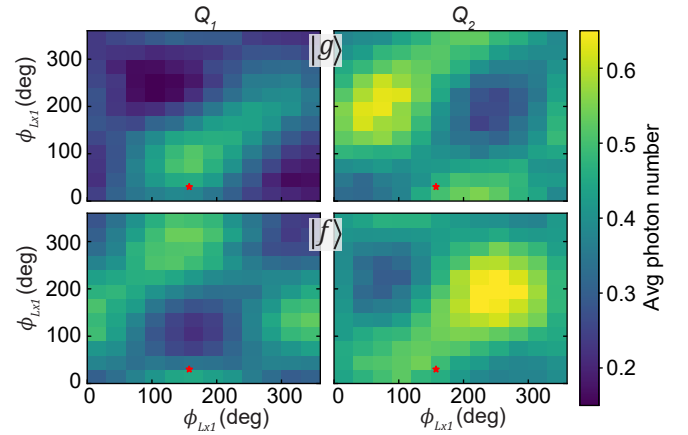


FIG. 16. Phase calibration for $|L_x\rangle$ preparation. Population of $|g\rangle$ (top) and $|f\rangle$ (bottom) on Q_1 (left) and Q_2 (right) are measured after $8\mu\text{s}$, and the red star marks the calibrated phase position.

prepare $|L_1\rangle$, a $(\pi/2)_{|gg\rangle\leftrightarrow|ee\rangle}$ pulse with some phase ϕ_{L1} followed by a $\pi_{|ee\rangle\leftrightarrow|ff\rangle}$ are applied through the flux line. These steps generally prepare $(|gf\rangle - e^{i\phi_{L0}}|fg\rangle)/\sqrt{2}$ and $(|gg\rangle - e^{i\phi_{L1}}|ff\rangle)/\sqrt{2}$. For non-zero $\{\phi_{L0}, \phi_{L1}\}$, $|ee\rangle$ is populated under the action of $\tilde{H}_{\text{static}}$, and we use this feature to find the correct preparation phases. We sweep the phase $\phi_{L0(1)}$ in the presence of all six tones and observe $|e\rangle$ population on both qutrits. The correct preparation phases are determined by values that minimize $|e\rangle$ population of both transmons during the first 8 μs of error correction, as presented in Fig. 15.

Preparation of $|L_x\rangle = (|L_0\rangle + |L_1\rangle)/\sqrt{2}$ does not require any sideband pulses as it is a product state $(|g\rangle - |f\rangle)(|g\rangle + |f\rangle)/2$. We apply a $(\pi/2)_{ge}$ pulse with a specific phase, followed by a π_{ef} pulse on both transmons. These pulses prepare the state $(|g\rangle + e^{i\phi_{Lx1}}|f\rangle)(|g\rangle + e^{i\phi_{Lx2}}|f\rangle)/2$, leaving two preparation phases ϕ_{Lx1} and ϕ_{Lx2} left for calibration. The correct phase combination can be calibrated on the 2D ϕ_{Lx1} - ϕ_{Lx2} phase sweep plot. Correct preparation phases will keep equal populations of $|g\rangle$ and $|f\rangle$ for both transmons at any time after turning on all sidebands. In Fig. 13e, both transmons' $|g\rangle$ and $|f\rangle$ populations are measured 8 μs after turning sidebands on. Fig. 16 shows the 2D phase sweep plot. This yields four phase coordinates $\{\phi_{Lx1}, \phi_{Lx2}\} = \{0, 180^\circ\} \otimes \{0, 180^\circ\}$, and two of the four correspond to $(|L_0\rangle \pm |L_1\rangle)/\sqrt{2}$. We distinguish the logical $|L_x\rangle$ by taking two-qutrit state tomography measurements after turning on the sidebands for 9 μs and choose the error-corrected case. The calibration process for the 4 QQ echo case is the same, except the QR sidebands are off.

Appendix H: Two qutrit tomography

Following the basis choice in Ref. 36, we apply 81 post rotations S_j from the tomography rotation set $S \otimes S$: $S = \{I, R_{ge}(0, \frac{\pi}{2}), R_{ge}(\frac{\pi}{2}, \frac{\pi}{2}), R_{ge}(0, \pi), R_{ef}(0, \frac{\pi}{2}), R_{ef}(\frac{\pi}{2}, \frac{\pi}{2}), R_{ef}(0, \pi), R_{ge}(0, \pi), R_{ef}(\frac{\pi}{2}, \frac{\pi}{2}), R_{ge}(0, \pi), R_{ef}(0, \pi), R_{ge}(0, \pi)\}$. Here I is the identity gate, and the rotations R_{ge} and R_{ef} are defined as follows

$$R_{ge}(\phi, \theta) = \begin{bmatrix} \cos \frac{\theta}{2} & -e^{-i\phi} \sin \frac{\theta}{2} & 0 \\ e^{i\phi} \sin \frac{\theta}{2} & \cos \frac{\theta}{2} & 0 \\ 0 & 0 & 1 \end{bmatrix}, \quad (\text{H1a})$$

$$R_{ef}(\phi, \theta) = \begin{bmatrix} 1 & 0 & 0 \\ 0 & \cos \frac{\theta}{2} & -e^{-i\phi} \sin \frac{\theta}{2} \\ 0 & e^{i\phi} \sin \frac{\theta}{2} & \cos \frac{\theta}{2} \end{bmatrix}. \quad (\text{H1b})$$

Simultaneous single-shot readouts are collected after each of the 81 rotations. Fig. 17 shows the single shot confusion matrix of our readout. To compensate for the measurement error, we applied the inverse of the confusion matrix to the readout result. Maximum-Likelihood-Estimation (MLE) is used to reconstruct the physical

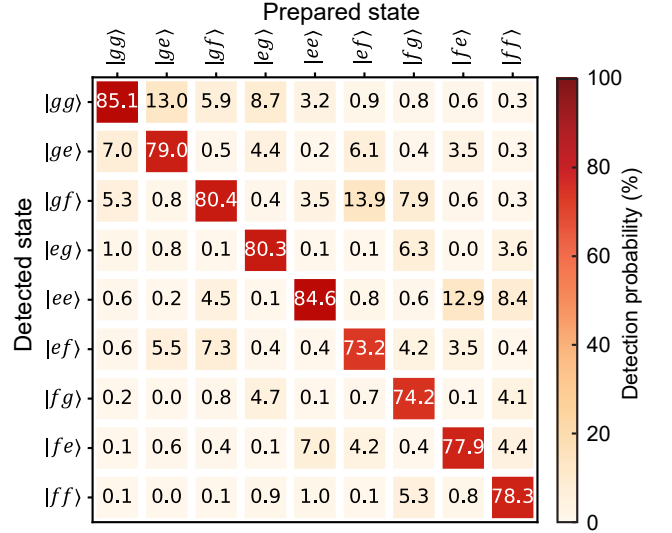


FIG. 17. Single shot confusion matrix. Two-qutrit basis states are prepared and measured 5000 times.

density matrix ρ_m that minimizes the cost function f_c ,

$$f_c(\vec{p}, \vec{q}) = \sum_{j=1}^{81} \sum_{a,b=g,e,f} \left(\frac{p_{j,|ab\rangle} - q_{j,|ab\rangle}}{q_{j,|ab\rangle}} \right)^2, \quad (\text{H2})$$

$$p_{j,|ab\rangle} = \langle ab | S_j \cdot \rho_m | ab \rangle,$$

$$q_{j,|ab\rangle} = \langle ab | S_j \cdot \rho_{exp} | ab \rangle.$$

Here $q_{j,|ab\rangle}$ is the measured probability for $|ab\rangle$ after the j th tomography rotation. For any state tomography data, we repeat the same experiment 5000 times to approximate each $q_{j,|ab\rangle}$. We first obtain ρ_{exp} from direct inversion of the experimental data and then perform MLE to find the physical density matrix ρ_m .

The tomographically reconstructed states after preparation, and after 9 μs for the three cases of free decay, 4 QQ echo, and AQEC are illustrated in Fig. 18. The evolution of fidelities as a function of time are shown in Fig. 19.

Appendix I: Simulation and error channels in the AQEC

All simulations are carried out in a Hamiltonian of dimension $3 \times 3 \times 2 \times 2$. We first simulate the theoretical lifetime improvement with only photon loss error in the rotating frame (Eq. B4), and results are shown in Fig. 20. All simulated data show improvements beyond the break-even point, even with only 10 μs T_1^{ge} and modest rate requirements for QQ and QR sidebands. The logical coherence limits come from the double photon loss event and off-resonant population to other stray states from the spectrum crowding (see Ref. [33]). Logical errors will happen when a second photon decays before correction.

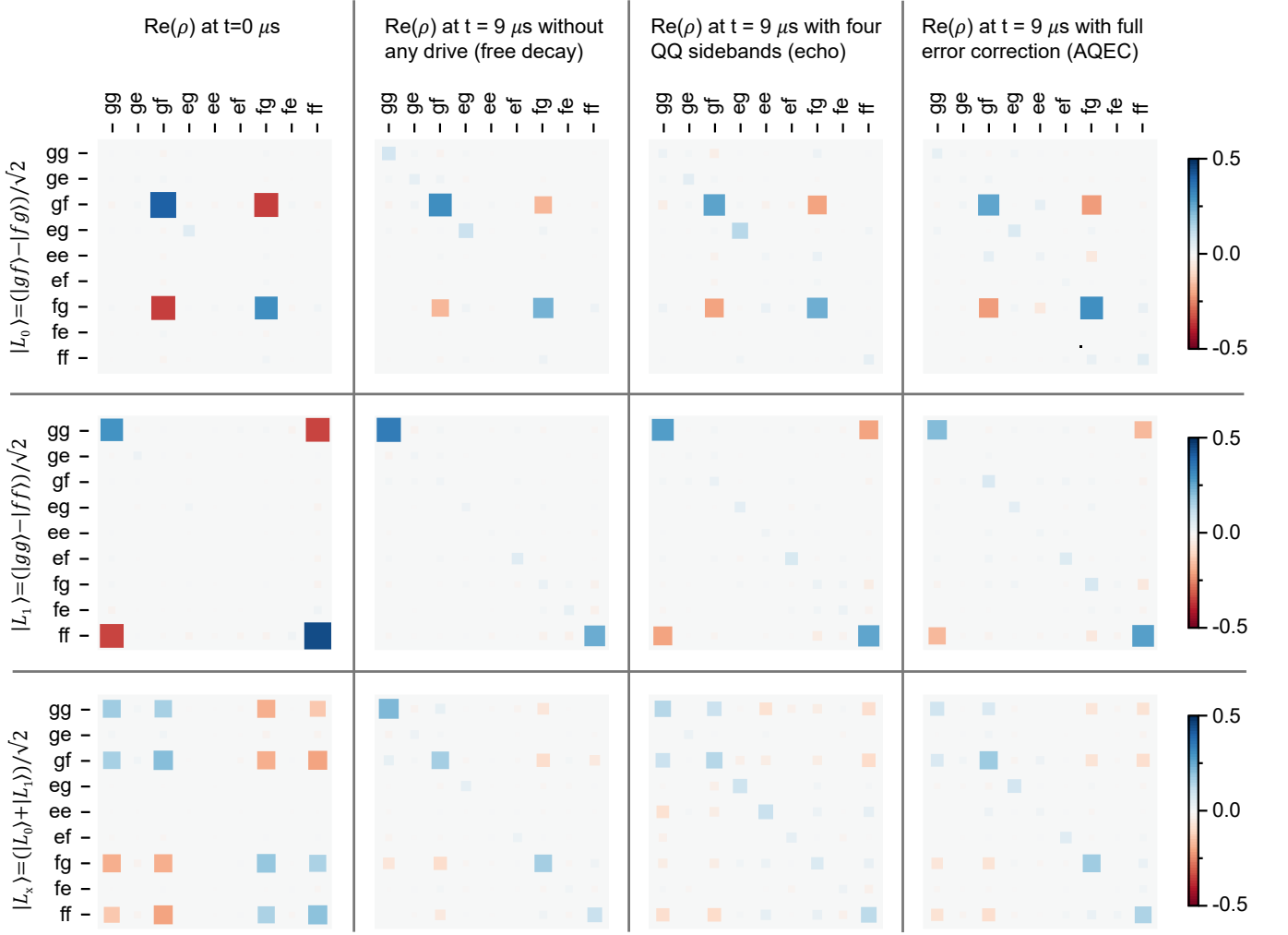


FIG. 18. Evolution of the logical states under different conditions. Panels from top to bottom correspond to the logical state $|L_0\rangle$, $|L_1\rangle$ and $|L_x\rangle$. The real part of the density matrices are plotted as the imaginary components are small after phase rotation. The left column shows the initial states. Improvements in the coherence can be seen for the echo case when compared to free decay. With the full Star code protocol, further improvements are observed.

$|L_x\rangle$ has a higher lifetime than $|L_j\rangle$ because it is partially protected against double photon loss in a single transmon. Longer physical T_1^{ge} , larger $W_{r/b}$, and Ω_j for a faster error correction rate help increase this limit.

To simulate the real system, several error channels are introduced in the static frame $\tilde{H}_{\text{static}}$ (Eq. B3)— single photon decay $T_1^{ge,j}$ and $T_1^{ef,j}$, single transmon dephasing T_ϕ^j , single-photon excitation T_1^\dagger , resonator photon population n_{res} and extra correlated dephasing $T_\phi^{|ff\rangle}$ at $|ff\rangle$ level. Since only ZZ_{ff1} and ZZ_{ff2} have effects on the logical state, we model the ZZs by directly adding energy shifts to $|fe\rangle$ and $|ef\rangle$, so that all logical basis still share the same energy and remain static in the frame. In the presence of external drives, the parameters will be different from the free decay case. We use experimentally measured ZZ_{ff1} and ZZ_{ff2} values in the simulation. The

full master equation is solved in QuTip,

$$\begin{aligned}
\frac{\partial \rho(t)}{\partial t} = & -i [H_{\text{full}}, \rho(t)] \\
& + \left(\sum_{j=1,2} \left(\frac{1}{T_1^{ge,j}} D_j[|g\rangle \langle e|] + \frac{1}{T_1^{ef,j}} D_j[|e\rangle \langle f|] \right) \right. \\
& + \frac{1}{T_1^\dagger} D_j[|e\rangle \langle g|] + \frac{2}{T_1^\dagger} D_j[|f\rangle \langle e|] \\
& \left. + \frac{1}{T_\phi^j} D_j[|e\rangle \langle e|] + \frac{4}{T_\phi^j} D_j[|f\rangle \langle f|] \right) \\
& + \kappa_j n_{\text{res}} D[a_{rj}^\dagger] + \kappa_j D[a_{rj}] \\
& + \frac{1}{T_\phi^{|ff\rangle}} D_{12}[|ff\rangle \langle ff|] \rho(t).
\end{aligned} \tag{11}$$

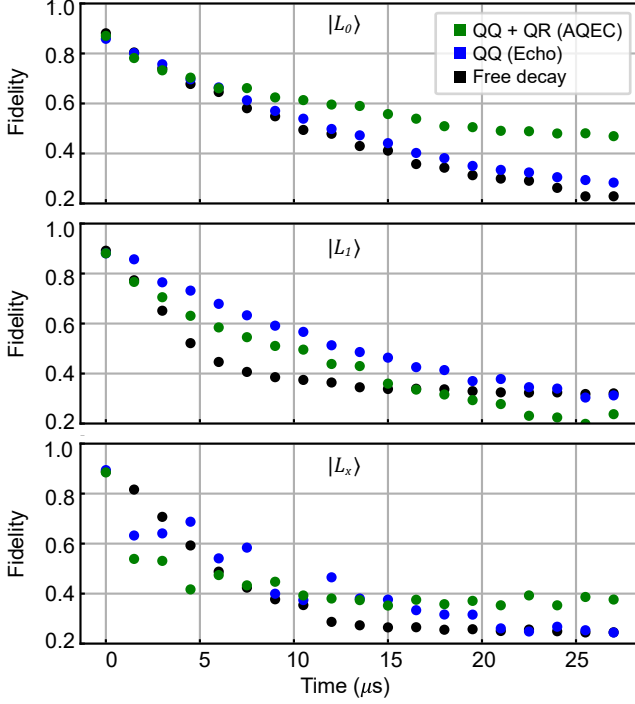


FIG. 19. Experimental logical state fidelity as a function of time. Fidelities are calculated at each time point through state tomography. $|L_1\rangle$ has higher fidelity in the free decay case because of contribution from $|gg\rangle$.

Here we define

$$H_{\text{full}} = \tilde{H}_{\text{static}} + \sum_{j=1,2} \chi_j n_{qj} n_{rj} + (ZZ_{ff1} |fe\rangle \langle fe| + ZZ_{ff2} |ef\rangle \langle ef|) \otimes I_4, \quad (12)$$

$$D[A]\rho = A\rho A^\dagger - \frac{1}{2} (A^\dagger A\rho + \rho A^\dagger A),$$

$$D_1[A] = D[A \otimes I_3 \otimes I_4],$$

$$D_2[A] = D[I_3 \otimes A \otimes I_4],$$

$$D_{12}[A] = D[A \otimes I_4].$$

Since transmons' anharmonicities are much larger than the transmon decay rate, each level's decay and dephasing are phase-independent. The system's full density matrix $\rho(t)$ is calculated and used to extract the coherence time and correctable error rate. Table IV includes all parameters used in the master equation simulation. For each separate case (free decay, 4 QQ echo, and AQEC), parameters are the same for all logical states $|L_0\rangle$, $|L_1\rangle$, and $|L_x\rangle$. T_ϕ^j is increased in the 4 QQ Echo and AQEC cases because of the echo suppression of $1/f$ noise.

Table V shows the lifetime limitations from different error channels in the AQEC case. In the ideal implementation, we include only the single photon decay and QR couplings χ_j in the simulation. The transmon photon excitation is enhanced when all sidebands are turned on. However, excitation error on $|L_x\rangle$ is partially correctable under three-level approximation, and thus $|L_x\rangle$ is more

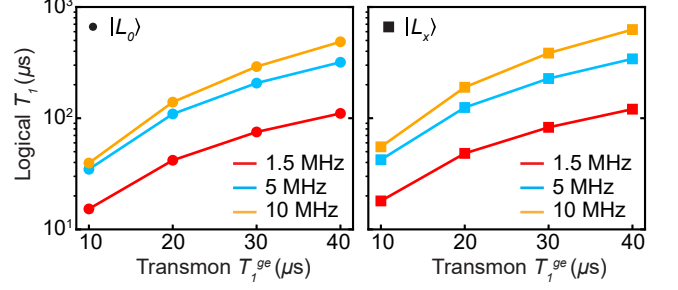


FIG. 20. Theoretical logical lifetime in the rotating frame. The logical lifetime increases as a function of physical T_1 . $|L_1\rangle$ has a similar lifetime as $|L_0\rangle$ in the simulation. A larger QQ sideband rate also provides higher logical qubit coherence. Parameter used for simulation are $\{W = 10, 5 \text{ MHz}, \Omega_j = 1.0 \text{ MHz}, \nu_r = -\nu_b = \frac{W}{2}\}$ with $\{W = 1.5 \text{ MHz}, \Omega_j = 0.4 \text{ MHz}, \nu_r = -\nu_b = 0.85 \text{ MHz}\}$, $\kappa = 0.5 \text{ MHz}$.

insensitive to it compared to $|L_{0/1}\rangle$. Resonator photon excitation happens from the heating effect when QR sidebands are on. Larger cavity photon number n_{res} will dephase all logical states and is one of the dominant error sources in our system. With higher resonator frequencies or an extra coupler between transmon and resonator, n_{res} can be reduced under the same QR rate Ω_j . The next two dominant error channels are cross-Kerr of between the transmons and QR frequency mismatch. ZZ_{ff1} and ZZ_{ff2} will dephase logical superposition states, as discussed in Appendix D (but has no effect on individual logical states). QR frequency mismatch is unavoidable in the presence of ZZ . In the experiment, we apply on-resonance $|e0\rangle \leftrightarrow |f1\rangle$ drive for $|L_0\rangle$ (corresponding the partner transmon being in $|g\rangle$). Consequently, for $|L_1\rangle$ the QR sidebands become detuned by ZZ_{ff1} and ZZ_{ff2} (corresponding to the partner being in $|f\rangle$) and effectively perform slower error correction. The QQ sideband frequency mismatch comes from a modest upper bound of the system's frequency drift (around 10 kHz). This is not comparable to the W and has no significant influence on the logical states. Other dephasing noise sources include $1/f$ noise, white noise, and $|ff\rangle$'s correlated dephasing. Among those three the white noise affects AQEC performance as it has a constant noise spectrum that cannot be suppressed through the spin echo. Star code protocol is also insensitive to small sideband amplitude drifts. The phase between logical states is defined by different sideband pairs, and amplitude drifts have to be comparable to W to change the logical states. Further, when all sidebands are on, both transmons' physical T_1 are shortened, which slightly reduces the performance. Other insignificant error sources include leakage to higher transmon energy levels ($|\alpha_j| \gg W$) and population in the coupler mode ($\omega_c \gg \omega_j$). Those are not considered in the simulation as the transition frequency is far away.

Simulation parameters	Free decay	4 QQ echo	AQEC
$Q_1 T_1^{ge,1} (\mu s)$	18.0	21.0	21.0
$Q_1 T_1^{ef,1} (\mu s)$	33.0	29.0	23.0
$Q_1 T_\phi^1 (\mu s)^\dagger$	15.0	23.0	23.0
$Q_1 T_1^\dagger (\mu s)$	∞	∞	600.0
$Q_2 T_1^{ge,2} (\mu s)^*$	8.0	9.0	9.0
$Q_2 T_1^{ef,2} (\mu s)$	33.0	29.0	23.0
$Q_2 T_\phi^2 (\mu s)^\dagger$	15.0	23.0	23.0
$Q_2 T_1^\dagger (\mu s)$	∞	∞	600.0
$T_\phi^{(ff)} (\mu s)$	4.4	80.0	80.0
κ_1 (MHz)	0.53	0.53	0.53
κ_2 (MHz)	0.48	0.48	0.48
χ_1 (MHz)			-0.2
χ_2 (MHz)			-0.2
n_{res}	0.00	0.00	0.03
W_r (MHz)		1.00	1.45
W_b (MHz)		1.70	1.25
ν_r (MHz)		1.50	0.80
ν_b (MHz)		0.00	-0.90
Ω_1 (MHz)			0.39
Ω_2 (MHz)			0.39
ZZ_{ff1} (MHz)			0.6
ZZ_{ff2} (MHz)			2.2

TABLE IV. Parameters used in the master equation simulation. $\{W_{r/b}, \Omega_j, \nu_{r/b}\}$ are extracted through Fig. 14 in simulation; ZZ_{ff1} and ZZ_{ff2} are experimentally measured through $|e0\rangle \leftrightarrow |f1\rangle$ on-resonance frequency difference when all sidebands on. Coherence times and χ_j in the simulations are tuned to explain the Star code experiment, which are slightly different from the measurement. Irrelevant parameters in each case are not shown in the table and not included in the simulation.

† Dephasing in the 4 QQ echo and AQEC cases are higher because of the QQ sideband spin-echo improvement.

* Q_2 's T_1^{ge} is lower than Q_1 's because of the TLSs around the transition frequency. Effects to the codewords performance are minimal as population on $|e\rangle$ is corrected.

Appendix J: Device Fabrication and Measurement Setup

The substrate for the device is a 430 μm thick C-plane sapphire wafer annealed at 1200°C for 2 hours. The ground plane uses 200 nm thick Tantalum film sputtered at 800°C. Large patterns, except Josephson junctions, were made through optical lithography and 20-second wet-etching in Transene Tantalum etchant 111. AZ 1518 was spin-coated as the positive photoresist, and a Heidelberg MLA 150 Direct Writer was used for the photolithography. The junction mask was fabricated with a Raith EBPG5000 Plus E-Beam Writer on a bi-layer resist (MMA EL11-950 PMMA A7). Transmon and coupler's Josephson junctions are Dolan bridge type. The mask was evaporated in a Plassys electron-beam evaporator with double-angle evaporation ($\pm 23^\circ$). The wafer was diced into 7×7 mm² chips and lifted off. After measuring the test junctions' resistances, the device was mounted on a printed circuit board, wire-bonded, pack-

aged inside a μ -metal shielded sample can, and installed inside a dilution fridge.

Figure 21 shows the room and cryogenic temperature measurement chain. The device is mounted on the mixing chamber plate of the dilution fridge with a 15 mK base temperature. A Tektronix 5014C AWG (1.2GSa/s) acts as the master trigger for all other equipment. The readout pulses are generated through two CW tones from RF sources (PSG-E8257D), modulated by AWG 5014C. The qubit input pulses are generated through another 4-channel AWG (Keysight M8195 65 Gsa/s, 16 Gsa/s per channel). The qubit and readout signals are combined and sent through lines In₁ and In₂ into the dilution fridge. Three DC sources (Yokogawa GS200) are used to bias the DC flux of the coupler and two Josephson Parametric Amplifiers (JPA). The red and blue QQ RF flux drives and two direct QR charge drives are synthesized through the same 4-channel AWG. Inside the fridge, at the 4K plate, all input lines have 20-dB attenuators. At the base plate, In₁ and In₂ lines have 10-dB attenuators, followed by a strong Eccosorb[®] providing 20-dB attenuation at 4 GHz. Charge₁ and Charge₂ lines have 20-dB attenuators, followed by strong Eccosorb providing 20-dB attenuation at 4 GHz, and a bandpass filter with passband 3.9 – 4.8 GHz. The DC Flux line has a low pass filter (DC – 1.9 MHz) and a weak Eccosorb (1-dB attenuation at 4 GHz). The red-frequency RF flux line passes through a weak Eccosorb first, followed by a high pass filter (cut off at 200 MHz) and a low pass filter (cut off at 2 GHz). The blue-frequency RF flux line passes through a weak Eccosorb first, followed by a high pass filter (cut off at 6 GHz). The two RF flux lines and the DC flux line are combined and pass through a Step Impedance Purcell Filter (SIPF) with a stop band 2.5 – 5.5 GHz. The two output signals go through three circulators, then each amplified by a JPA with 15-dB gain, followed by a low pass filter (cut off at 8 GHz), two circulators, a DC block, and amplified with one LNF High-Electron-Mobility Transistor (HEMT) amplifier. The output signals are further amplified at room temperature, then demodulated, filtered with a low pass filter (DC – 250 MHz), and amplified again using the SRS Preamplifier. The final signal is digitized with Alazar ATS 9870 (1GSa/s) and analyzed in a computer.

Error channels limit	$ L_0\rangle$	$ L_1\rangle$	$ L_x\rangle$
Ideal implementation*	95 μ s		160 μ s
Transmon photon excitation	~ 360 μ s		~ 3 ms
n_{res} dephasing [†]	~ 55 μ s		~ 25 μ s
Other dephasing noise [†]	~ 50 μ s		~ 25 μ s
Transmon ZZ dephasing	∞		~ 25 μ s
QR frequency mismatch	> 10 ms	~ 45 μ s	~ 25 μ s
QQ frequency mismatch	> 10 ms		~ 1.5 ms
QQ rate mismatch	> 10 ms		~ 4 ms
Reduced physical T_1	~ 330 μ s		~ 400 μ s
Experimental lifetime	23.4 ± 6.8 μ s	16.9 ± 3.7 μ s	8.7 ± 4.6 μ s

TABLE V. Various decoherence channels for the logical qubit. Ideal implementation represents logical states' lifetime with QR coupling and only T_1 error. Each limit is extracted using the simulation through lifetime difference after adding relevant error channels. The average photon number in the resonator (n_{res}) increases during external drives and dephases transmons through photon shot noise. Other dephasing noise include $1/f$ noise, white noise, correlated dephasing noise, and any other noise source. The total effect is represented with T_ϕ^j in the simulation. ZZ between transmons introduces a large mismatch in QR frequency for $|L_1\rangle$ and $|L_x\rangle$, and the effect is combined with ZZ dephasing for $|L_x\rangle$ case. The drifts in sideband amplitudes frequencies are less than 5% and 20 kHz, and those limits are in the order of ms.

* Ideal implementation includes QR couplings χ_j but no QQ ZZ couplings.

[†] n_{res} and T_ϕ^j are determined through simulation-experiment matching.

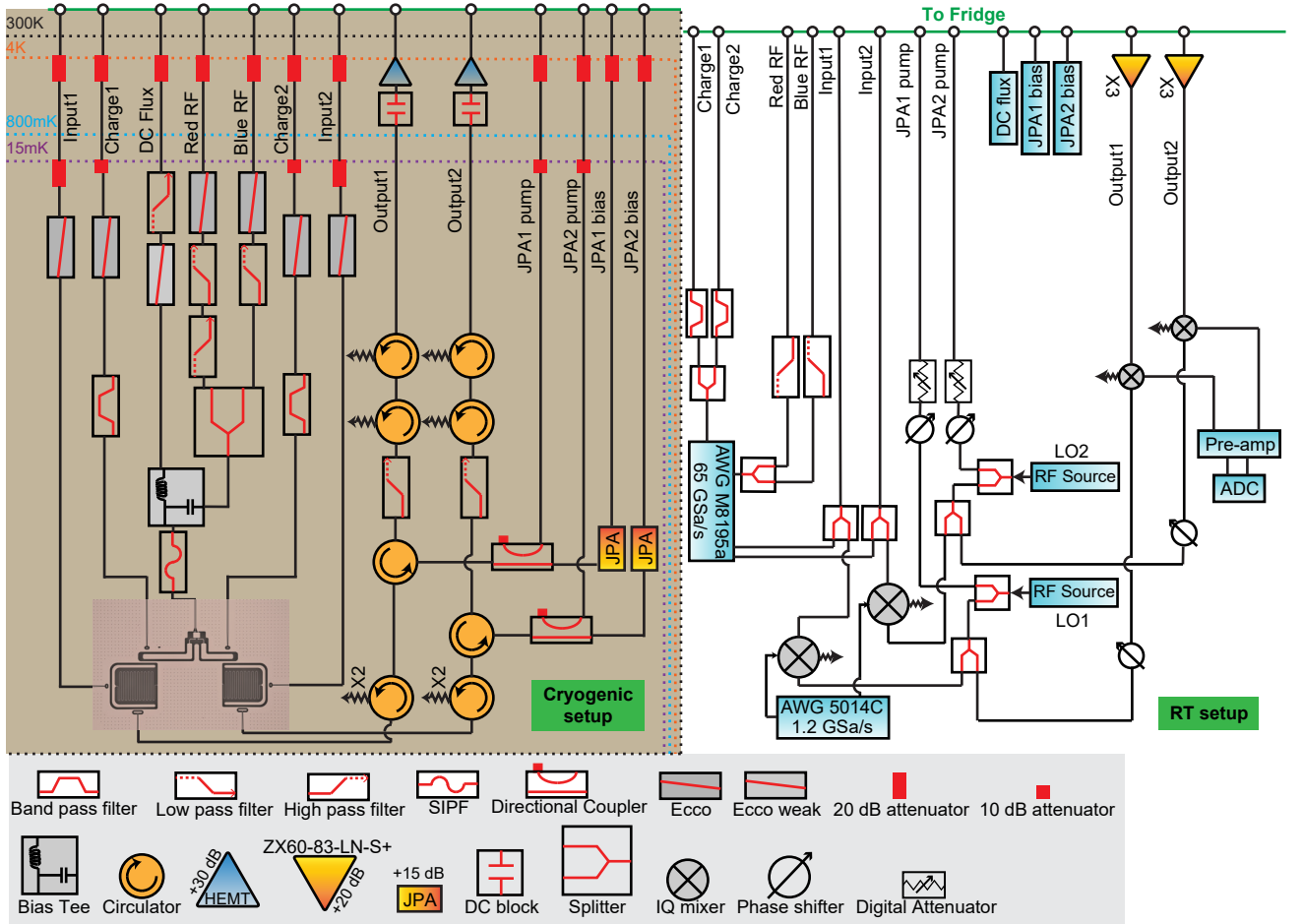


FIG. 21. Detailed cryogenic and room temperature measurement setup.

-
- [1] P. W. Shor, Polynomial-time algorithms for prime factorization and discrete logarithms on a quantum computer, *SIAM Journal on Computing* **26**, 1484 (1997).
- [2] A. Aspuru-Guzik, A. D. Dutoi, P. J. Love, and M. Head-Gordon, Simulated quantum computation of molecular energies, *Science* **309**, 1704 (2005).
- [3] S. Krinner, N. Lacroix, A. Remm, A. Di Paolo, E. Genois, C. Leroux, C. Hellings, S. Lazar, F. Swiadek, J. Herrmann, G. J. Norris, C. K. Andersen, M. Müller, A. Blais, C. Eichler, and A. Wallraff, Realizing repeated quantum error correction in a distance-three surface code, *Nature* **605**, 669 (2022).
- [4] M. H. Abobeih, Y. Wang, J. Randall, S. J. H. Loenen, C. E. Bradley, M. Markham, D. J. Twitchen, B. M. Terhal, and T. H. Taminiau, Fault-tolerant operation of a logical qubit in a diamond quantum processor, *Nature* **606**, 884 (2022).
- [5] D. Bluvstein, H. Levine, G. Semeghini, T. T. Wang, S. Ebadi, M. Kalinowski, A. Keesling, N. Maskara, H. Pichler, M. Greiner, V. Vuletić, and M. D. Lukin, A quantum processor based on coherent transport of entangled atom arrays, *Nature* **604**, 451 (2022).
- [6] L. Egan, D. M. Debroy, C. Noel, A. Risinger, D. Zhu, D. Biswas, M. Newman, M. Li, K. R. Brown, M. Cetina, and C. Monroe, Fault-tolerant control of an error-corrected qubit, *Nature* **598**, 281 (2021).
- [7] C. Ryan-Anderson, J. G. Bohnet, K. Lee, D. Gresh, A. Hankin, J. P. Gaebler, D. Francois, A. Chernoguzov, D. Lucchetti, N. C. Brown, T. M. Gatterman, S. K. Halit, K. Gilmore, J. A. Gerber, B. Neyenhuis, D. Hayes, and R. P. Stutz, Realization of real-time fault-tolerant quantum error correction, *Phys. Rev. X* **11**, 041058 (2021).
- [8] A. Erhard, H. Poulsen Nautrup, M. Meth, L. Postler, R. Stricker, M. Stadler, V. Negnevitsky, M. Ringbauer, P. Schindler, H. J. Briegel, R. Blatt, N. Friis, and T. Monz, Entangling logical qubits with lattice surgery, *Nature* **589**, 220 (2021).
- [9] J. Cramer, N. Kalb, M. A. Rol, B. Hensen, M. S. Blok, M. Markham, D. J. Twitchen, R. Hanson, and T. H. Taminiau, Repeated quantum error correction on a continuously encoded qubit by real-time feedback, *Nature Communications* **7**, 11526 (2016).
- [10] J. Kelly, R. Barends, A. G. Fowler, A. Megrant, E. Jeffrey, T. C. White, D. Sank, J. Y. Mutus, B. Campbell, Y. Chen, Z. Chen, B. Chiaro, A. Dunsworth, I.-C. Hoi, C. Neill, P. J. J. O'Malley, C. Quintana, P. Roushan, A. Vainsencher, J. Wenner, A. N. Cleland, and J. M. Martinis, State preservation by repetitive error detection in a superconducting quantum circuit, *Nature* **519**, 66 (2015).
- [11] G. Waldherr, Y. Wang, S. Zaiser, M. Jamali, T. Schulte-Herbrüggen, H. Abe, T. Ohshima, J. Isoya, J. F. Du, P. Neumann, and J. Wrachtrup, Quantum error correction in a solid-state hybrid spin register, *Nature* **506**, 204 (2014).
- [12] P. Schindler, J. T. Barreiro, T. Monz, V. Nebendahl, D. Nigg, M. Chwalla, M. Hennrich, and R. Blatt, Experimental repetitive quantum error correction, *Science* **332**, 1059 (2011).
- [13] F. Verstraete, M. M. Wolf, and J. Ignacio Cirac, Quantum computation and quantum-state engineering driven by dissipation, *Nature Physics* **5**, 633 (2009).
- [14] Z. Wang, T. Rajabzadeh, N. Lee, and A. H. Safavi-Naeini, Automated discovery of autonomous quantum error correction schemes, *PRX Quantum* **3**, 020302 (2022).
- [15] V. V. Albert, S. O. Mundhada, A. Grimm, S. Touzard, M. H. Devoret, and L. Jiang, Pair-cat codes: autonomous error-correction with low-order nonlinearity, *Quantum Science and Technology* **4**, 035007 (2019).
- [16] E. Kapit, Error-transparent quantum gates for small logical qubit architectures, *Phys. Rev. Lett.* **120**, 050503 (2018).
- [17] J.-M. Lihm, K. Noh, and U. R. Fischer, Implementation-independent sufficient condition of the knill-laflamme type for the autonomous protection of logical qubits by strong engineered dissipation, *Phys. Rev. A* **98**, 012317 (2018).
- [18] E. Kapit, Hardware-efficient and fully autonomous quantum error correction in superconducting circuits, *Phys. Rev. Lett.* **116**, 150501 (2016).
- [19] J. Cohen and M. Mirrahimi, Dissipation-induced continuous quantum error correction for superconducting circuits, *Phys. Rev. A* **90**, 062344 (2014).
- [20] M. Mirrahimi, Z. Leghtas, V. V. Albert, S. Touzard, R. J. Schoelkopf, L. Jiang, and M. H. Devoret, Dynamically protected cat-qubits: a new paradigm for universal quantum computation, *New Journal of Physics* **16**, 045014 (2014).
- [21] Z. Leghtas, G. Kirchmair, B. Vlastakis, R. J. Schoelkopf, M. H. Devoret, and M. Mirrahimi, Hardware-efficient autonomous quantum memory protection, *Phys. Rev. Lett.* **111**, 120501 (2013).
- [22] M. Sarovar and G. J. Milburn, Continuous quantum error correction by cooling, *Phys. Rev. A* **72**, 012306 (2005).
- [23] E. Knill, R. Laflamme, and L. Viola, Theory of quantum error correction for general noise, *Phys. Rev. Lett.* **84**, 2525 (2000).
- [24] J. M. Gertler, B. Baker, J. Li, S. Shirol, J. Koch, and C. Wang, Protecting a bosonic qubit with autonomous quantum error correction, *Nature* **590**, 243 (2021).
- [25] A. Grimm, N. E. Frattini, S. Puri, S. O. Mundhada, S. Touzard, M. Mirrahimi, S. M. Girvin, S. Shankar, and M. H. Devoret, Stabilization and operation of a kerr-cat qubit, *Nature* **584**, 205 (2020).
- [26] P. Campagne-Ibarcq, A. Eickbusch, S. Touzard, E. Zalys-Geller, N. E. Frattini, V. V. Sivak, P. Reinhold, S. Puri, S. Shankar, R. J. Schoelkopf, L. Frunzio, M. Mirrahimi, and M. H. Devoret, Quantum error correction of a qubit encoded in grid states of an oscillator, *Nature* **584**, 368 (2020).
- [27] Y. Ma, Y. Xu, X. Mu, W. Cai, L. Hu, W. Wang, X. Pan, H. Wang, Y. P. Song, C.-L. Zou, and L. Sun, Error-transparent operations on a logical qubit protected by quantum error correction, *Nature Physics* **16**, 827 (2020).
- [28] L. Hu, Y. Ma, W. Cai, X. Mu, Y. Xu, W. Wang, Y. Wu, H. Wang, Y. P. Song, C.-L. Zou, S. M. Girvin, L.-M. Duan, and L. Sun, Quantum error correction and universal gate set operation on a binomial bosonic logical qubit, *Nature Physics* **15**, 503 (2019).
- [29] N. Ofek, A. Petrenko, R. Heeres, P. Reinhold, Z. Leghtas, B. Vlastakis, Y. Liu, L. Frunzio, S. M. Girvin, L. Jiang, M. Mirrahimi, M. H. Devoret, and R. J. Schoelkopf, Ex-

- tending the lifetime of a quantum bit with error correction in superconducting circuits, *Nature* **536**, 441 (2016).
- [30] J. Koch, T. M. Yu, J. Gambetta, A. A. Houck, D. I. Schuster, J. Majer, A. Blais, M. H. Devoret, S. M. Girvin, and R. J. Schoelkopf, Charge-insensitive qubit design derived from the Cooper pair box, *Physical Review A* **76**, 042319 (2007).
- [31] E. Kapit, M. Hafezi, and S. H. Simon, Induced self-stabilization in fractional quantum hall states of light, *Phys. Rev. X* **4**, 031039 (2014).
- [32] E. Kapit, The upside of noise: engineered dissipation as a resource in superconducting circuits, *Quantum Science and Technology* **2**, 033002 (2017).
- [33] Z. Li, T. Roy, D. Rodríguez Pérez, E. Kapit, and D. I. Schuster, a very small logical qubit (vslq) in the star code operation, unpublished.
- [34] Y. Lu, S. Chakram, N. Leung, N. Earnest, R. K. Naik, Z. Huang, P. Groszkowski, E. Kapit, J. Koch, and D. I. Schuster, Universal stabilization of a parametrically coupled qubit, *Phys. Rev. Lett.* **119**, 150502 (2017).
- [35] A. Wallraff, D. I. Schuster, A. Blais, J. M. Gambetta, J. Schreier, L. Frunzio, M. H. Devoret, S. M. Girvin, and R. J. Schoelkopf, Sideband transitions and two-tone spectroscopy of a superconducting qubit strongly coupled to an on-chip cavity, *Phys. Rev. Lett.* **99**, 050501 (2007).
- [36] R. Bianchetti, S. Filipp, M. Baur, J. M. Fink, C. Lang, L. Steffen, M. Boissonneault, A. Blais, and A. Wallraff, Control and tomography of a three level superconducting artificial atom, *Phys. Rev. Lett.* **105**, 223601 (2010).
- [37] T. Roy, Z. Li, E. Kapit, and D. I. Schuster, Tomography in the presence of stray inter-qubit coupling, arXiv preprint arXiv:2103.13611 (2021).
- [38] D. Rodríguez Pérez, Quantum error mitigation and autonomous correction using dissipative engineering and coupling techniques, *ProQuest Dissertations and Theses*, 147 (2021).
- [39] Y. Zhao, Y. Ye, H.-L. Huang, Y. Zhang, D. Wu, H. Guan, Q. Zhu, Z. Wei, T. He, S. Cao, F. Chen, T.-H. Chung, H. Deng, D. Fan, M. Gong, C. Guo, S. Guo, L. Han, N. Li, S. Li, Y. Li, F. Liang, J. Lin, H. Qian, H. Rong, H. Su, L. Sun, S. Wang, Y. Wu, Y. Xu, C. Ying, J. Yu, C. Zha, K. Zhang, Y.-H. Huo, C.-Y. Lu, C.-Z. Peng, X. Zhu, and J.-W. Pan, Realization of an error-correcting surface code with superconducting qubits, *Phys. Rev. Lett.* **129**, 030501 (2022).
- [40] S. P. Chitta, T. Zhao, Z. Huang, I. Mondragon-Shem, and J. Koch, Computer-aided quantization and numerical analysis of superconducting circuits (2022).
- [41] M. Roth, M. Ganzhorn, N. Moll, S. Filipp, G. Salis, and S. Schmidt, Analysis of a parametrically driven exchange-type gate and a two-photon excitation gate between superconducting qubits, *Phys. Rev. A* **96**, 062323 (2017).
- [42] J. Chu, D. Li, X. Yang, S. Song, Z. Han, Z. Yang, Y. Dong, W. Zheng, Z. Wang, X. Yu, D. Lan, X. Tan, and Y. Yu, Realization of superadiabatic two-qubit gates using parametric modulation in superconducting circuits, *Phys. Rev. Applied* **13**, 064012 (2020).
- [43] M. Ganzhorn, G. Salis, D. J. Egger, A. Fuhrer, M. Mergenthaler, C. Müller, P. Müller, S. Paredes, M. Pechal, M. Werninghaus, and S. Filipp, Benchmarking the noise sensitivity of different parametric two-qubit gates in a single superconducting quantum computing platform, *Phys. Rev. Research* **2**, 033447 (2020).
- [44] E. A. Sete, N. Didier, A. Q. Chen, S. Kulshreshtha, R. Manenti, and S. Poletto, Parametric-resonance entangling gates with a tunable coupler, *Phys. Rev. Applied* **16**, 024050 (2021).
- [45] T. Brown, E. Doucet, D. Ristè, G. Ribeill, K. Cicak, J. Aumentado, R. Simmonds, L. Govia, A. Kamal, and L. Ranzani, Trade off-free entanglement stabilization in a superconducting qutrit-qubit system, *Nature Communications* **13**, 3994 (2022).
- [46] J. C. Gallop and B. W. Petley, SQUIDS and their applications, *Journal of Physics E: Scientific Instruments* **9**, 417 (1976).
- [47] T. Roy, Z. Li, E. Kapit, and D. I. Schuster, Realization of two-qutrit quantum algorithms on a programmable superconducting processor, arXiv preprint arXiv:2211.06523 (2022).